TURUN YLIOPISTON JULKAISUJA
ANNALES UNIVERSITATIS TURKUENSIS

SARJA - SER. A I OSA - TOM. 432

ASTRONOMICA - CHEMICA - PHYSICA - MATHEMATICA

THE EFFECT OF VARIOUS DOPING METHODS ON SUPERCONDUCTING PROPERTIES OF PULSED LASER DEPOSITED $YBa_2Cu_3O_{7-\delta}$ THIN FILMS

by

Matti Irjala

TURUN YLIOPISTO
UNIVERSITY OF TURKU
Turku 2011

From the Wihuri Physical Laboratory
Department of Physics and Astronomy
University of Turku
Turku, Finland
and
National Graduate School in Materials Physics
Helsinki, Finland

Supervised by

Professor Petriina Paturi
Wihuri Physical Laboratory
Department of Physics and Astronomy
University of Turku
Turku, Finland

Reviewed by

Dr. Vitaliy V. Yurchenko
University of Oslo
Department of Physics
P. O. Box 1048
Blindern
0316 Oslo
Norway

Dr. Jens Hänisch
Institut für Metallische Werkstoffe
IFW Dresden
Helmholtzstr. 20
01069 Dresden
Germany

Opponent

Dr. Adrian Crisan
School of Metallurgy and Materials
University of Birmingham
Edgbaston, Birmingham
B15 2TT
United Kingdom

ISBN 978-951-29-4818-5 (PRINT)
ISBN 978-951-29-4819-2 (PDF)
ISSN 0082-7002
Painosalama Oy - Turku, Finland 2011

Acknowledgments

This work has been carried out in the years 2007–2011 in the Wihuri Physical laboratory at the Department of Physics and Astronomy, University of Turku. The Graduate School of Materials Research, National Graduate School of Materials Physics, Turku University Foundation, Prof. Väino Hovi Foundation and Jenny and Antti Wihuri Foundation are acknowledged for financial support.

I would like to express my sincere gratitude for my supervisors Prof. P. Paturi and Dr. H. Huhtinen for giving me the opportunity to work in this research group and the guidance and help that I have received during this work. Their patience and expertise have made this possible. Also, I would like to thank Prof. Emer. R. Laiho for the fruitful discussions and advice I have received.

I express my gratitude to my opponent Dr. A. Crisan: it is my privilege to have you as my opponent. Drs. V. Yurchenko and J. Hänisch are acknowledged for reviewing the thesis. All co-authors, especially Drs. V. P. S. Awana and M. Falter, are gratefully acknowledged for their vital contributions and support.

I want to thank my colleagues Dr. T. Suominen, Dr. K. Schlesier, MSc I. Ojala, MSc H. Palonen, MSc S. Tuominen and MSc E. Takala for all the shared moments, in and out of laboratory. The entire group of Superconductivity and Magnetism has truly provided a motivating and relaxed, yet highly scientific enviroment during these years. Thank you all.

To my friends, it is impossible to name everyone I am grateful to. Thank you for standing by my side despite the circumstances and pushing me through the hard times. I am especially fortunate to know all of you. One measure of friendship consists not in the number of things friends can discuss, but in the number of things they need no longer mention. You know who you are.

Also, I want to thank my brothers Heikki and Mikko and their families for all the shared moments together. As a little brother I have had the privilege to follow my brothers' example and enjoy their care during my childhood and adulthood. Thank you.

And finally, my deepest gratitude goes to my parents, without whom none of this would have happened. Thank you mother and father for everything.

Abstract

In this work, three different methods of doping superconducting films have been studied; cationic substitution of Pr^{3+} (Pr) in Y^{3+} site and non-superconducting perovskites $BaMO_3$ (M = Ce, Zr) (BCO and BZO, respectively), to investigate their effect on structural and superconducting properties in pulsed laser deposited $YBa_2Cu_3O_{7-\delta}$ (YBCO) thin films. Also, both micro- and nanograined YBCO were used to investigate their difference in anisotropic and high-field properties. Structural properties were investigated with atomic force microscopy (AFM) and X-ray diffraction (XRD), in addition with earlier transmission electron microscopy (TEM) results. Superconducting properties were measured with the magnetometry and electrical transport of angular dependency of critical current density J_c up to 8 T and down to 10 K, together with electrical transport on a pulse magnet setup up to 30 T at temperatures between 65 and 88 K.

Pr inclusion was found to decrease all the superconducting properties in samples on STO. However, in samples on NiW and MgO both J_c and the superconducting transition temperature, T_c, increased for low dopant concentrations ($< 4\%$). J_c increased for low concentrations of Pr at temperatures above 60 K in samples on MgO substrates and at all temperatures and fields in samples on buffered NiW substrates. This increase is related to the increase in grain boundary critical current density J_c^{gb}.

BCO doping increased J_c, and the highest values were obtained with 2 – 4 wt% of dopant concentration, depending on temperature and external magnetic field. The structural measurements and angular dependency of J_c indicate that BCO grows cube-on-cube forming randomly distributed nanoparticles in the YBCO lattice, with a size of ≈ 2 nm, therefore giving rise to isotropic pinning. Also, the angular anisotropy of J_c was found to decrease with BCO inclusion. In contrast, BZO grows epitaxially cube-on-cube with YBCO, forming a correlated network of film penetrating nanorods. The thin films ablated from the nanograined target together with the BZO-doped nanograined target were found to have greatly decreased angular anisotropy of J_c, compared to thin films deposited from the micrograined target. This is due to the excess number of lattice defects, mostly dislocations, caused by smaller growth islands in samples deposited from nanograined YBCO, and nanorods in BZO-doped samples. Moreover, the optimal BZO concentration was found to increase above 20 T and in samples on NiW substrate. In high fields, this is connected to a model where isotropic pinning sites are formed in addition to nanorods, and in samples on NiW to a higher lattice defect density.

Articles included in this thesis

[**P1**] M. Irjala, H. Huhtinen, P. Paturi, Anuj Kumar, V. P. S. Awana, A. V. Narlikar and R. Laiho, *Optimization of the Pr concentration in $Y_{1-x}Pr_xBCO$ films prepared by pulsed laser deposition*, Journal of Physics: Conference Series, **153** (2009) 012014

[**P2**] M. Irjala, H. Huhtinen, V. P. S. Awana, M. Falter and P. Paturi, *Increased grain boundary critical current density J_c^{gb} by Pr-doping in pulsed laser deposited $Y_{1-x}Pr_xBCO$ thin films*, Journal of Applied Physics, **In Print** (2011)

[**P3**] M. Irjala, H. Huhtinen, R. Jha, V. P. S. Awana and P. Paturi *Optimization of the $BaCeO_3$ concentration in YBCO films prepared by pulsed laser deposition*, IEEE Transactions on Applied Superconductivity, **21** (2011) 2762

[**P4**] P. Paturi, M. Irjala and H. Huhtinen, *Greatly decreased critical current density anisotropy in $YBa_2Cu_3O_{6+x}$ thin films ablated from nanocrystalline and $BaZrO_3$-doped nanocrystalline targets* , Journal of Applied Physics, **103** (2008) 123907

[**P5**] H. Huhtinen, M. Irjala, P. Paturi, M. A. Shakhov and R. Laiho, *Influence of $BaZrO_3$ dopant concentration on properties of $YBa_2Cu_3O_{6+x}$ films in magnetic fields up to 30 T*, Journal of Applied Physics, **107** (2010) 053906

[**P6**] H. Huhtinen, M. Irjala, P. Paturi and M. Falter, *Optimal BZO Doping in YBCO Films Grown on Single Crystal STO and Buffered NiW Substrates*, IEEE Transactions on Applied Superconductivity, **21** (2011) 2753

My contribution to the publications is as follows. I have deposited the samples in [**P1**]–[**P3**] using readily available targets, measured and analysed both the structural and superconducting measurements and authored the papers. In [**P4**]–[**P5**] I have done the photo-lithography and AFM analysis of the patterned samples. In [**P5**]–[**P6**], I have performed the magnetic measurements and in [**P4**]–[**P6**] I have participated in the authoring of the manuscripts. In [**P6**], I also prepared the NiW substrates for the deposition process.

Articles relevant to this work but not included in this thesis

[**P7**] H. Huhtinen, A. Välimäki, M. Irjala, P. Paturi, Y. Y. Tse and R. Laiho, *Effect of $BaZrO_3$ Dopants in (110)-Oriented $YBa_2Cu_3O_{6+x}$ Thin Films*, IEEE Transactions on Applied Superconductivity, **19 (3)** (2009) 3412

[**P8**] P. Paturi, M. Irjala, A. B. Abrahamsen and H. Huhtinen *Defining B_c, B^* and B_ϕ for YBCO Thin Films*, IEEE Transactions on Applied Superconductivity, **19 (3)** (2009) 3431

[**P9**] P. Paturi, M. Irjala, H. Huhtinen and A. B. Abrahamsen *Modeling flux pinning in thin undoped and $BaZrO_3$-doped YBCO films*, Journal of Applied Physics, **105** (2009) 023904

[**P10**] H. Huhtinen, M. Irjala, P. Paturi, J. C. Grivel, Y. Y. Tse, M. Falter, J. Eickemeyer, Y. Zhao, *Growth and BZO-doping of the nanostructured YBCO thin films on buffered metal substrates*, Physica C, **470** (2010) S1013

[**P11**] H. Huhtinen, M. Irjala, P. Paturi and M. Falter *The effect of BZO doping concentration and thickness dependent properties of YBCO films grown by PLD on buffered NiW substrates*, Physica C, **In Print** (2011)

[**P12**] H. Huhtinen, M. Irjala and P. Paturi *Magnetic field dependent photoinduced superconductivity and its oxygen-deficient dependency in undoped and BZO-doped YBCO thin films*, Proc. of European Conference on Applied Superconductivity EUCAS 2011,
Physics Procedia, **Submitted** (2011)

Contents

1 Introduction

"All science is either physics or stamp collecting."
–Ernest Rutherford

1.1 Superconductivity

1.1.1 Description and history

Superconductivity in a material is defined by two criteria: firstly, its electrical resistivity is zero below the superconducting critical temperature, T_c. Secondly, the material is a perfect diamagnet below T_c, meaning that the susceptibility of the material, χ, is -1, which again means that the magnetic field cannot penetrate the superconductor. If a material fulfills these two criteria, it is called a superconductor. Depending on T_c, superconductors are classified as low-temperature and high-temperature superconductors. Depending on the diamagnetic behaviour, the comminution continues into a type 1 and type 2 in low-temperature superconductors (LTSC). All high-temperature superconductors (HTSC) are of type 2. These classifications are discussed later on.

For the first time, superconductivity was observed in 1911 by a Dutch scientist, Heike Kamerlingh Onnes, when he was measuring the resistivity of Mercury [1]. Onnes observed that at 4.2 K the resistivity of Hg dropped to zero. In the following decades, more superconducting materials were found, e.g. lead and aluminium. Later, in 1933, Meissner and Ochsenfeld discovered the perfect diamagnetism [2], and this phenomenon was named after them. The first phenomenological explanation for the Meissner–Ochsenfeld effect was provided by Fritz and Heinz London in 1935 [3], when they proposed that the magnetic field penetrates the superconductor, decreasing exponentially and the depth where it becomes equal to $1/e$ times that of the magnetic field on the surface of the superconductor is called the London penetration depth, λ. Further understanding of superconductivity emerged in the 1950's as the phenomenological Ginzburg–Landau [4] and the microscopic Barden–Cooper–Schrieffer (BCS) [5] theories were presented. In brief, the BCS theory explains why two electrons couple into Cooper pairs, the charge carriers of a supercurrent. The Ginzburg–Landau theory describes the behaviour of superconductors near T_c. It presents a new parameter, the coherence length, ξ, which is the shortest distance within which a considerable change in the Cooper pair density can take place. The ratio between λ and ξ is the Ginzburg–Landau parameter κ,

$$\kappa = \frac{\lambda}{\xi}, \tag{1}$$

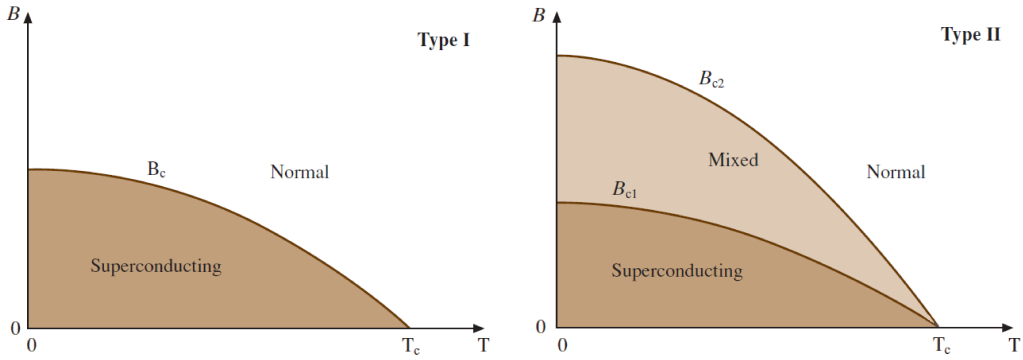

Figure 1. Schematic $T - B$ phase diagrams for the type 1 and type 2 superconductors [10].

which defines the classification to types 1 and 2.

Before 1986, most of the superconducting materials were pure metals or alloys, with a T_c below 30 K, which is the BCS theory limit for T_c. We now call all these materials low-temperature superconductors. The field was revolutionized in 1986, when Bednorz and Müller found superconductivity above 30 K in the La-Ba-Cu-O system [6], whereafter also other superconducting cuprates were found. T_c of these materials is above 30 K, and moreover, even as high as 135 K (under normal pressure) for $HgBa_2Ca_2Cu_3O_{8+\delta}$. The first superconducting material above the boiling point of nitrogen (77 K), $YBa_2Cu_3O_{7-\delta}$ (YBCO, T_c= 92 K) was found in 1987 by Wu *et al.* [7]. Even though high-temperature superconductivity has recently been found e.g. in MgB_2 [8] and Fe-As compounds [9], cuprates are still the only superconducting materials above the boiling point of liquid nitrogen.

Superconductors are divided into type 1 and type 2, depending on the diamagnetic behaviour and whether κ is smaller or larger than $1/\sqrt{2}$, respectively [4]. The schematic phase diagrams are presented in figure 1. The Meissner–Ochsenfeld effect works as described earlier only in type 1 superconductors. In type 1, superconductivity is limited by an external magnetic field, the critical field B_c. When B_c is exceeded, magnetic field penetrates the whole sample, the superconducting phase is lost and, therefore, material returns to the normal state. Almost all pure bulk metals are type 1 superconductors, but remarkably the best conductors at room temperature (Ag, Au and Cu) do not become superconducting at all. Type 1 superconductors are modeled well by the BCS theory which relies upon electron pairs coupled by lattice vibration interactions [5].

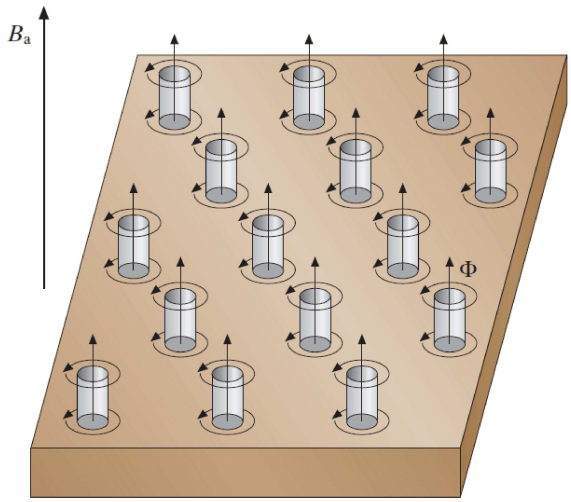

Figure 2. In the mixed state, magnetic flux quanta penetrate the superconductor as vortices. Each vortex consists of a single fluxoid $\phi_0 = h/(2e)$. The applied external magnetic field is presented as B_a [10].

Type 2 superconductors have two critical field values, B_{c1} and B_{c2}. Below B_{c1}, the magnetic field cannot penetrate the material and it behaves like type 1 superconductor. Above B_{c1}, but below B_{c2}, magnetic field penetrates the material as magnetic flux quanta and the material is in a mixed state. The magnetic flux quantum, $\phi_0 = h/(2e) = 2.07 \cdot 10^{-15}$ Wb, which is called a vortex, creates a non-superconducting region in the vortex area, but leaves the rest of the sample in a superconducting state. A schematic description of the mixed state is presented in figure 2. Above B_{c2}, the material is in the normal state and the magnetic field penetrates the whole sample [10]. The critical field values are typically much higher in type 2 than in type 1, therefore type 2 materials are superior in high magnetic fields. All high-temperature superconductors are of type 2. As a result, the superconducting phase diagram of a type 2 superconductor is more complex than type 1's, as figure 1 presents. The BCS theory also explains type 2 superconductivity, excluding the coupling mechanism in HTSC's, which is still under dispute.

1.1.2 Applications and motivation

Superconductivity has many important applications in electronics [11], magnet and power applications [12], e.g. in magnet resonance imaging (MRI), electromagnets, radio frequency (RF) cavities, power transmission cables, transformers, fault current limiters and motors. High quality high-temperature superconductor (HTSC) thin films with strong magnetic flux pinning can also be used to reduce microwave losses in RF filters [13]. HTSC's, and especially cuprates, benefit from the high critical fields and high T_{c}, which enables the usage in high magnetic fields and cooling with liquid nitrogen. Compared with liquid helium cooling, liquid nitrogen is notably cheaper. The price per liter of liquid nitrogen is approximately one hundredth of the price per liter of liquid helium. The upper critical field, B_{c2}, can be extremely high in HTSC's, > 100 T at low temperatures and for YBCO, B_{c2} is still 30 T even at 77 K [14], while in type 1, the superconductivity is lost at relatively low field values, $\ll 1$ T. Moreover, the irreversibility field, B_{irr} ($B_{\mathrm{c1}} < B_{\mathrm{irr}} < B_{\mathrm{c2}}$), which is the upper limit for loss-free current transport, is very high in cuprates. The irreversibility line, $B_{\mathrm{irr}}(T)$, is presented later in figure 4. Due to these reasons, HTSC materials are interesting from an application point of view, as they can operate in the high field region at relatively high temperatures. However, the most significant problem with HTSC's is the difficulty of the synthesis and the brittle ceramic structure. MgB_2 does present an exception from this, but its T_{c} is still relatively low, 39 K [8].

Power transmission cables, transformers, and motors are some of the important applications using YBCO. However, due to the complex structure of the cuprates, their superconducting properties are highly anisotropic and the critical current density, J_{c}, is perniciously limited by grain-boundaries. Nonetheless, J_{c} can be increased in the high-field region by introducing artificial pinning centres into the structure. For example, doping the YBCO film with non-superconducting perovskites $BaMO_3$ (M = metal) or other nanosized particles has been widely studied. These challenges have driven the research further and [**P1**]– [**P6**] discuss the enhancement of pinning by both columnar and point defects, as well as the grain-boundary problem.

For [**P1**]–[**P2**], our earlier results on bulk samples of $Y_{1-x}Pr_x$BCO (x = 0 - 0.20) [15] showed an increase in J_{c} up to $x = 0.08$. Therefore, studies with thin films were conducted. Also, the similarity between cationic dopants Pr^{3+} and Ca^{2+}, where Ca^{2+} is well known to increase the grain boundary critical current density $J_{\mathrm{c}}^{\mathrm{gb}}(B)$ [16–18], motivated us to study the possible GB effect with Pr^{3+} [**P2**]. In [**P3**], cubic perovskite $BaCeO_3$ (BCO) dopant was used. BCO has been found to be a beneficial dopant for

YBCO in melt-textured, bulk and metal-organic chemical deposited (MOD) samples [19–24], but no systematic study with pulsed laser deposited (PLD) thin films had been performed. The most widely studied cubic perovskite dopant, $BaZrO_3$ (BZO), was used in [**P4**]–[**P6**]. BZO is a very promising dopant, as it can create correlated nanorods in YBCO films, which are 5-10 nm in diameter and penetrate the whole film, forming columnar defects [25–27]. These nanorods induce a wide peak in the $B \parallel c$ direction in the angular dependency of J_c and increase J_c significantly in the high-field region [28]. Therefore J_c's angular dependency measurements [**P4**], high-field optimization of dopant concentration [**P5**] and comparison between samples ablated on both single crystal and technical substrates [**P6**] were performed. Moreover, nanocrystalline pulsed laser deposition targets were used in [**P4**]–[**P6**] to investigate the difference between samples deposited from microcrystalline targets (μ-film) and nanocrystalline targets (n-film).

HTSC coated conductors (CC) are currently under development as a very promising second generation HTSC wire that is able to fulfil all the necessary requirements; bendable design, high J_c and mass production at reasonable expenses [29]. CC's use biaxial texturing technology of YBCO films on long technical metallic substrates. In [**P2**] and [**P6**] such technical substrates, buffered NiW substrates, provided by Zenergy Power GmbH were used.

1.2 $YBa_2Cu_3O_{7-\delta}$

Yttrium barium copper oxide, $YBa_2Cu_3O_{7-\delta}$ (YBCO) has been widely studied since its discovery. It is one of the $ReBa_2Cu_3O_{7-\delta}$ (Re = Y, Pr, Nd, Sm, Eu, Gd, Ho ...) compounds, of which only PrBCO is not superconducting. YBCO is the material of choice for the second generation wires, CC's mainly due to the extremely high B_{irr}, 10 T at 77 K [**P5**], but also because of the high T_c, 92 K [7]. Some of the selected parameters for YBCO are presented in table 1. All the cuprate superconductors are extreme type 2 with κ values of $\simeq$100. The crystal structure of YBCO is shown in figure 3. The unit cell of YBCO contains double CuO_2 layers with embedded yttrium ions. Slightly different positions (in the c-direction) of the Cu and O atoms lead to buckling in the CuO_2 planes. The oxygen atoms occupy perovskite-like anion positions halfway between the copper atoms. These square-coordinated CuO_2 layers are a characteristic feature of all cuprate superconductors. Neighbouring CuO_2 blocks are separated by two Ba–O layers. The Cu–O chains between the two Ba–O layers in the b-direction are a special feature of the YBCO compound [10].

Table 1. Selected properties for YBCO. Critical fields from [30] and [14], lattice parameters from [31], coherence and penetration lengths from [32].

T_c(K)	$B_{c2,c}$(T)	$B_{c2,ab}$(T)	$B_{c2,c}^{77K}$(T)	
92	122	674	30	
a(nm)	b(nm)	c(nm)	λ_{ab}(nm)	ξ_{ab}(nm)
0.3823	0.3887	1.168	130	1.3

The properties of the YBCO depend strongly on the oxygen content. With $\delta > 0.6$, YBCO has a tetragonal $P4/mmm$ structure and is an antiferromagnetic insulator at low temperatures [33]. In contrast, with $\delta < 0.6$, the lattice structure is orthorhombic $Pmmm$ and YBCO is superconducting. With $\delta < 0.2$, T_c above 90 K is achieved with lattice parameters $a = 0.3823$ nm, $b = 0.3887$ nm and $c = 1.168$ nm [31] and between $0.2 < \delta < 0.6$ lowered superconducting properties are observed. The double CuO_2 layers with embedded yttrium ions are called conduction planes, as superconductivity lies in the planes. The Cu-O chains in the c-axis direction act as charge reservoirs, which provide carriers for the CuO_2 planes. This complex structure also leads to the strong anisotropy of the superconducting properties. Perpendicular to these planes ($c-$axis direction), resistivity is notably higher in the normal state and semiconducting behaviour can be detected [34]. Also, J_c depends strongly on the crystallographic direction of the external magnetic field (θ). For undoped YBCO deposited from the common μ-crystalline target, the most characteristic feature in $J_c(\theta)$ is a concave shape with a peak at $H \parallel ab$ ($\theta = 90°$) [35]. This is due to the intrinsic pinning of Ba–O layers and extended defects parallel to the ab-planes [36]. This subject will be covered later in this thesis.

1.3 Pinning of magnetic flux

In type 2 superconductors, as described earlier, magnetic flux penetrates the material as flux quanta between B_{c1} and B_{c2}, and this state is called the mixed state. Figure 4 presents a schematic description of the vortex phase diagram for HTSC. Vortices can form three distinct phases in HTSC: vortex lattice, glassy vortex state and vortex liquid [37]. Vortex lattice represents almost perfect crystalline structure, vortex glass is strongly disordered vortex solid and vortex liquid is a disordered phase, where thermal

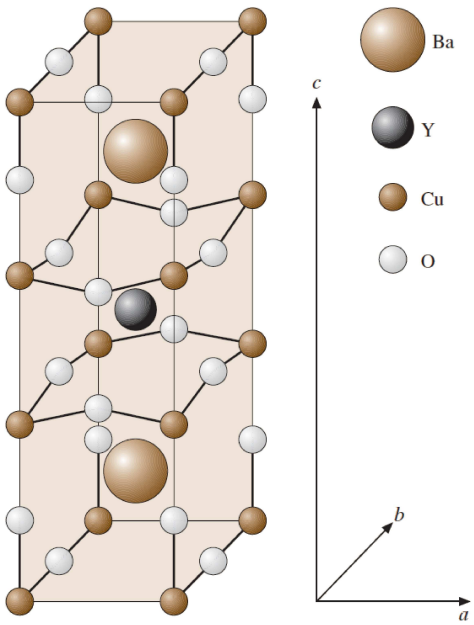

Figure 3. Unit cell of the orthorhombic $YBa_2Cu_3O_{7-\delta}$ [10].

fluctuations destroy the crystalline order. The vortex lattice can melt e.g. with increasing temperature and near B_{c2} vortex liquid phase is observed [37]. Generally, J_c decreases with increasing temperature and magnetic field and reaches zero at the melting line, also called irreversibility line, B_{irr}. Above this line, the superconductor does not carry loss-free current, although, it is still in a superconducting state [38].

In the presence of a magnetic field perpendicular to the current direction, a Lorentz force $F_L = j \times \phi_0$, where j is the current and ϕ_0 is the magnetic flux quantum, acts on the vortices and as long as the F_L is smaller than the pinning force F_p, vortices do not move. Now, if a current is applied, as figure 5 presents, vortices move according to the F_L, dissipating energy which can be observed as resistance. In a case of a defect-free sample (fig. 5a) vortices move according to the F_L. In the presence of point defect pinning (fig. 5b), vortices are partially pinned. If columnar defects parallel to the applied magnetic field are introduced (fig. 5c), the entire sections of vortices are pinned and this is an example of strong pinning [37]. In real film samples, there is always more than one type of defect present.

When the pinning forces F_p are not strong enough to prevent flux motion, the superconductor is called soft; otherwise it is called hard. As the transport current is present,

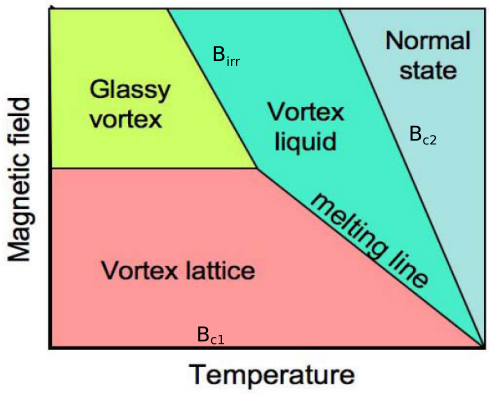

Figure 4. Schematic vortex phase diagram for a HTSC [38].

F_{L}, together with thermal fluctuations, acts to depin the vortices and induce a collective flux motion. This very slow flux motion is called a thermally activated flux creep [37] when the F_{p} dominates, and when F_{L} dominates, the faster motion is called a flux flow [37].

Only if vortices are immobilized by a counteracting F_{p}, a superconductor can sustain high J_{c}. However, the higher the current density, the greater F_{L} acting on the vortices. J_{c} is essentially the point at which the F_{L} begins to exceed the maximum available F_{p} [39]. The F_{p} is generated from the presence of lattice defects, which create potential energy wells for vortices. Size, shape, composition and structural interaction between the lattice and the defect define F_{p} of a single defect. These pinning sites can be divided into natural pinning sites, e.g. intrinsic pinning of the CuO_2 planes in YBCO and lattice defects formed during the sample deposition process, and artificial pinning centres (APC's), which can be obtained e.g. by doping superconducting materials with various non-superconducting foreign materials (e.g. [26, 40, 41]), substrate decoration (e.g. [42–45]) or through heavy-ion radiation (e.g. [46, 47].)

1.3.1 Natural pinning sites

Many thin film defects have been proposed to act as pinning sites in YBCO. Figure 6 presents the possible crystalline defects present in YBCO thin films. Precipitates are commonly grown secondary phases (e.g. Y_2O_3). Twin boundaries (TB's) are always planar defects and due to the orthorhombic structure of YBCO. In-plane misoriented grains and grain boundaries (GB's) are common in CC substrates because of the imper-

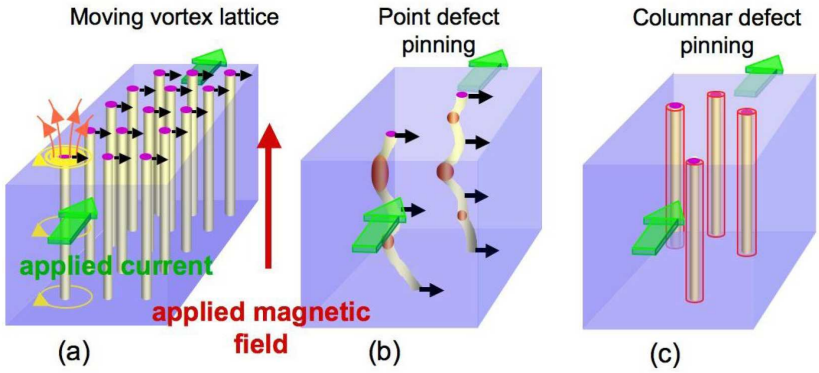

Figure 5. A simplified illustration of vortices moving under the Lorentz force F_{L} (black arrows), induced by an applied current (green arrow) in the presence of an external magnetic field (red arrow) perpendicular to the film surface. a) A defect-free sample. b) Vortices are partially pinned by point defects. c) Entire sections of vortices are pinned by columnar defects. In real film samples, there is always more than one type of defect present [38].

fect crystalline texture of the substrate [39]. The linear defects such as screw dislocations evolve in the centre of growth islands, and therefore they have nonrandom distribution in the film. They also act as strong pinning sites [48, 49]. Threading dislocations result e.g. around screw dislocations, between misoriented grains and growth islands because of the imperfect lattice matching between YBCO and the substrate, which is also the reason for misfit dislocations. The surface roughness is due to a multitude of effects, including columnar growth, porosity and strain, and it usually increases with film thickness. The antiphase boundaries form if e.g. in the growth process film domains coalesce with the layers matching yttrium-to-barium, and so forth. In vapour deposition, voids can appear as a consequence of surface roughness when shadowing or reduced mobility prevent vapour from filling valleys. The out-of-plane misoriented grains are usually caused by film roughness, a tilted substrate structure, other substrate defects and too low deposition temperature. Planar defects $\parallel ab$ are usually GB's, TB's, non-123 phases of YBCO or stacking faults. Precipitates are agglomerations of a large number of atoms; in contrast, point defects are atomic-scale disruptions in the crystal structure. The latter can be in the form of vacancies or interstitials (missing or extra atoms), or impurities. Point defects also result in YBCO when yttrium and barium change places [39] and e.g. oxygen vacancies are typical point defects in YBCO.

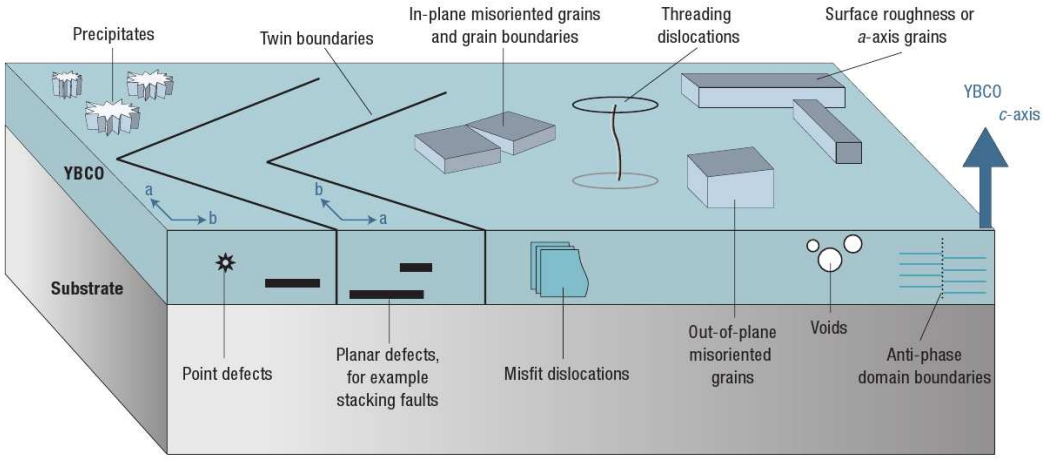

Figure 6. Many thin-film defects have been proposed as flux pinning sites in YBCO; anything that locally disturbs the crystalline perfection over a scale of 0.1–1 nm is a candidate, but the effective pinning centres have a cross section approximately equal to the coherence length ξ [50]. Strain fields associated with defects may also pin vortices [39].

In general, one can affect the formation of these defects via deposition process parameters and the choice of the substrate. This matter will be covered later in this thesis.

J_c is generally 10-100 times higher in epitaxial YBCO films than in YBCO single crystals because of the natural defects [50]. One possibility to increase J_c is to tune the deposition to obtain the optimal number of effective natural pinning sites. This can be done e.g. by using nanocrystalline PLD targets, as in [**P4**]–[**P6**]. The challenge is to reveal which of these film defects are most effective for pinning vortices. However, the relationship between defects and J_c is complex and pinning is not simply additive. By increasing the number of effective pinning sites, J_c can be increased up to a certain limit, but beyond that limit superconducting properties decrease with increasing defect density. Even further beyond superconductivity disappears due to the de-pairing current where Cooper pairs break up.

1.3.2 Artificial pinning centres

According to their dimensionality, APC's can be classified into 1D–3D, as figure 7 presents. 1D-APC's can be e.g. dislocations or columnar defects, like BZO-nanorods in [**P4**]–[**P6**]. 2D-APC's are e.g. low angle grain boundaries (which is a borderline case as

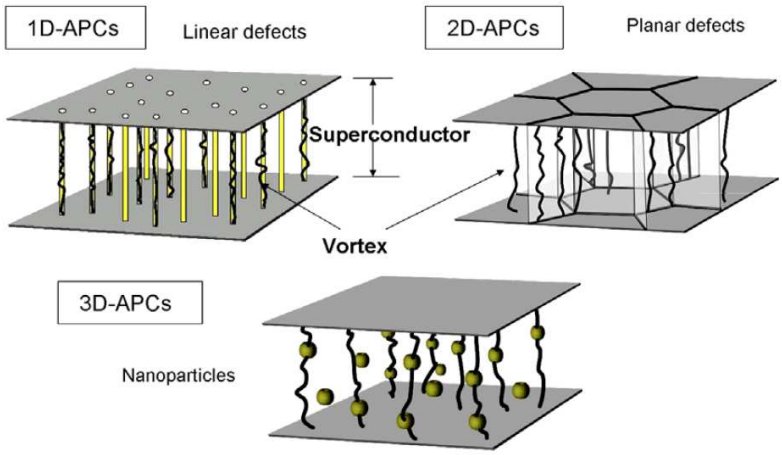

Figure 7. An illustration of the dimensionality of artificial pinning centres (APC's): 1D-APC's, 2D-APC's, and 3D-APC's [29].

it consists of lines of dislocations), discussed in [**P2**], twin planes, discussed in [**P4**], or anti-phase boundaries [51]. 3D-APC's are nanoparticles ([**P3**]), secondary phases, etc. Also, the defects smaller than ξ should be classified into 0D-APC's, and e.g. vacancies [52] and cation disorders [53] are of this type. Cationic substitution of Pr^{3+} (in Y^{3+} site) in [**P1**]–[**P2**] is an example of 0D-APC.

There are various methods of making APC's. The method used in works [**P1**]–[**P6**]was to mix the desired dopant (Pr^{3+}, $BaZrO_3$, $BaCeO_3$) with YBCO into the PLD target and control the growth of the APC's inside the matrix with the PLD parameters. Other possible methods include substrate decoration [44], where the SC matrix is grown on top of an intentionally affected surface, heavy ion irradiation [54], where the film matrix is damaged, producing columnar defects, and multilayering [55] where SC and APC layers alternate.

Because of the lattice mismatch with YBCO, APC's, e.g. BZO can also induce the formation of natural pinning sites in thin films [25], where the YBCO lattice around the BZO particle is distorted and e.g. edge dislocations can be observed. Creating APC's is generally a compromise between increased flux pinning and e.g. decreased T_c due to increased lattice distortion, and therefore the amount of dopant together with the deposition process has to be optimized for the desired result.

1.4 Models

1.4.1 Bean model

The Bean critical-state model [56, 57] provides a phenomenological description for the hysteretic magnetization of type 2 superconductors in a varying external magnetic field. As the magnetic field penetrates the superconductor as vortices, the magnetization depends on the vortex distribution. In the Bean model the distribution of vortices is determined by the balance between electromagnetic driving forces and forces pinning the vortices to material defects. It assumes that the current flows always at the critical density, J_{c}, and that the internal magnetic field is given by the Maxwell curl equation,

$$\nabla \times B = \mu_0 J_{\mathrm{c}}, \tag{2}$$

where B is the magnetic field density, μ_0 is the permeability of vacuum and J_{c} is the critical current density. In the case of rectangular thin film samples in [**P1**]–[**P3**], [**P5**] and [**P6**], J_{c} can be calculated with

$$J_{\mathrm{c}} = \frac{2\Delta m}{a(1 - a/3b)V} \qquad \text{for } a \leq b, \tag{3}$$

where a and b are the length and width of the sample, V is the volume of the sample and Δm is the opening of the hysteresis loop [58]. This method gives J_{c} with good accuracy, especially in thin films with B parallel to the short dimension [59]. Moreover, though J_{c} does not depend on the field in the Bean model, it gives a good estimation of $J_{\mathrm{c}}(B)$ [60].

The pinning force, F_{p}, set limits on the amount of supercurrent that can be applied through the superconductor. In the Bean model, F_{p} has its maximum magnitude at the edge of the sample, given by [14]

$$F_{\mathrm{p}} = J_{\mathrm{c}} B_0, \tag{4}$$

where B_0 is the applied magnetic field. Hence, large F_{p} produces large J_{c} and vice versa.

1.4.2 Field dependence of J_{c} – a power law

In the case of strong pinning, where e.g. the entire vortex length fits into the pinning site, the field range where vortex bundles are pinned by a single pinning site [37], can be separated from the single-vortex pinning by accommodation field [61]

$$B^* = \frac{4\varepsilon_r}{\varepsilon_0} B_\phi, \tag{5}$$

where $B_\phi = n\phi_0$ is the matching field (the density of vortices equals with the density of linear defects), ε_r is the pinning energy and ε_0 is the vortex energy scale [37]

$$\varepsilon_0 = \left(\frac{\phi_0}{4\pi\lambda}\right)^2. \tag{6}$$

This result applies to low temperatures. At higher temperatures, the ε_r's temperature dependence should be taken into account. However, in experimental studies, B^* is generally defined by [62, 63]

$$\frac{J_\mathrm{c}(B^*)}{J_\mathrm{c}(0)} = 0.9. \tag{7}$$

The field dependence of J_c above B^* can be described by the power law

$$J_\mathrm{c}(B) = A(T)B^{-\alpha(T)}, \tag{8}$$

where $A(0\ \mathrm{T})$ is proportional to $J_\mathrm{c}(0\ \mathrm{T})$ and the exponent α varies depending on the F_p. The definition of the field dependence can also be formulated with B^α, when α has negative values. Therefore, α values are considered as absolute values in this thesis. According to theories [49, 64, 65], $\alpha = 0.5$ and 0.625 are connected to a low density of strong pinning centres in intermediate field range. In high magnetic field range, $\alpha = 1.0$ is predicted [64]. Lowered $\alpha = 0.2 - 0.4$ is observed in samples with strong vortex pinning, where J_c is less field dependent and vortex-vortex interaction lowers the potential wells of the pinning sites, in contrast to the vortices being pinned in between the pinning sites, as happens above the matching field B_ϕ [66].

The dependence of the resistivity on temperature and magnetic field in the transition can be expressed by a function

$$\rho(T, B) \propto e^{-U(B)/T}, \tag{9}$$

where $U(B) = U_0/B^\alpha$ is the power law dependent pinning potential [67]. At constant temperature and in measurement geometry of [**P5**], where a maximum Lorentz force configuration with $B \parallel c$ is used, $\rho(B)$ can be expressed as

$$\rho(B) = \rho_0 e^{-U_0/TB^\alpha}, \tag{10}$$

where ρ_0 is the normal state resistivity.

1.4.3 Angular dependence of J_c – Blatter scaling

To determine the magnetic and temperature dependences of the isotropic and anisotropic pinning contributions of YBCO films, the so-called Blatter scaling theory [37, 68] can

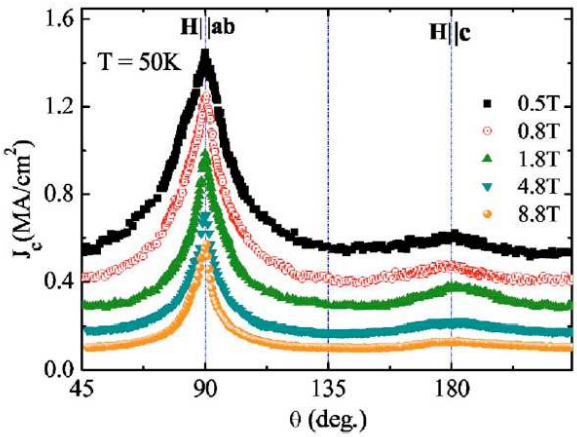

Figure 8. Angular dependence of J_c for the YBCO sample at 50 K in several magnetic fields [35].

be applied. Recently a new model for $J_c(\theta)$ has also been presented [69–71]. This so-called Long's model considers anisotropy due to pinning through a statistical process, whereas Blatter takes into consideration the intrinsic anisotropy of HTSC. However, Blatter scaling theory was used in this work because the effective anisotropy parameter $\gamma_{\rm eff}$ was one of the main interests and the Blatter scaling provides it easily.

In figure 8 is presented the J_c–θ results from Gutierrez et. al. [35] at 50 K for an undoped YBCO film in five different external magnetic fields, where the characteristic shape of $J_c(\theta)$ curve with a peak at $B \parallel ab$ ($\theta = 90°$) is observed. This sharp increase of J_c is due to electron mass anisotropy, intrinsic pinning and also for other extrinsic linear or planar defects lying parallel to the ab-planes, e.g. stacking faults. A smoother and weaker peak at $B \parallel c$ ($\theta = 180°$) is typical for PLD films and it is connected to the anisotropic pinning centres, e.g. threading dislocations, twin boundaries and grain boundaries in c-direction [72–74]. At high fields, i.e. above the matching field $B_\phi \approx 5$ T [75] for optimally BZO-doped (4 wt%) YBCO, and at high temperatures the c-axis peak disappears or weakens strongly. Above B_ϕ the point pinning sites interact with the columnar pinning sites and a porous vortex solid forms [76], resulting in the concave shape of the J_c–θ curve.

The methodology presented here is based on applying the Blatter scaling approach [37] to the J_c data of figure 8 for different magnetic fields at a given temperature, and identify the regions where J_c collapses when plotted as the function of the effective

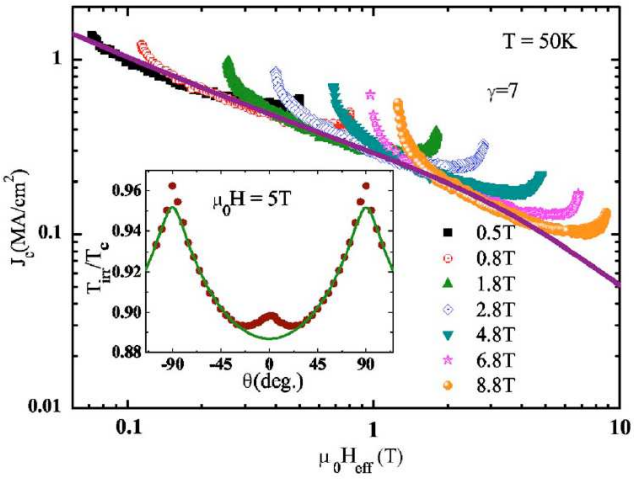

Figure 9. $J_c(\theta)$ as a function of $H_{\rm eff}$ for γ=7, at 50 K and for different magnetic fields. The solid line is J_c dependence with $H_{\rm eff}$ obtained from the collapsed regions. The inset shows the anisotropy of the irreversibility line at $\mu_0 H = 5$ T [35].

magnetic field

$$B_{\rm eff} = B\sqrt{\cos^2(\theta) + \gamma^{-2}\sin^2(\theta)}, \tag{11}$$

where B is the magnetic field density, θ is the angle between the magnetic field and the c-axis, and γ is the anisotropy parameter of the material, connected to the electronic mass anisotropy [37]. Figure 9 presents the $J_c(\theta)$ as a function of $B_{\rm eff}$ for γ=7, from figure 8. The solid line is J_c dependence with $B_{\rm eff}$ obtained from the collapsed regions. The inset shows the anisotropy of the irreversibility line at $\mu_0 H = 5$ T. The obtained $\gamma = 5 - 7$ is a typical value for undoped μ-crystalline YBCO [35], but the approach to choose an effective anisotropy $\gamma_{\rm eff}$ has been used recently to describe the anisotropy in YBCO films [35, 73, 77]. Even though the intrinsic electron mass anisotropy is the same, $\gamma_{\rm eff}$ takes into account the random pinning sites and extra columnar pinning sites, and therefore $\gamma_{\rm eff}$ is typically smaller e.g. for BZO-doped samples and other samples with excess number of strong pinning sites. Hence, smaller $\gamma_{\rm eff}$ represents decreased J_c anisotropy due to extra pinning sites. As presented later in figure 37, the data fall into a line for BZO-doped YBCO with $\gamma_{\rm eff} = 1.5$, which is notably smaller than with the undoped sample deposited from μ-crystalline target, whereas with $\gamma_{\rm eff} = 5$ data do not fall in line with BZO-doped sample, although there is no reason to assume a change in the electronic mass anisotropy.

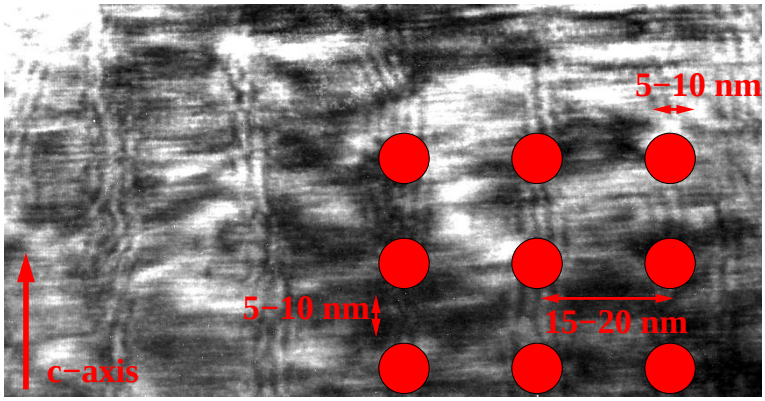

Figure 10. TEM picture shows c-axis aligned nanorods for 3.9 wt% BZO-doped sample, with 5-10 nm of diameter and 15-20 nm of spacing. The nanorods are roughly half occupied by BZO particles with distorted YBCO in between [25].

1.4.4 Transmission electron microscopy

Earlier transmission electron microscopy (TEM) measurements [25] have shown a network of correlated pinning sites in undoped n-films and also in 3.9 wt% BZO-doped n-film samples (figure 10) there is a network of film penetrating and c-axis aligned nanorods with 5-10 nm of diameter and 15-20 nm of spacing. Also, the areal density of BZO-rods, calculated from the planar view images, was found to be 1300, 2500 and 4200 μm^2 for 2.9, 3.9 and 9,0 wt% of BZO, respectively, showing that the dependence is not linear. For 3.9 wt% doped sample the nanorods are roughly half occupied by BZO particles with distorted YBCO in between. Also, the YBCO lattice is well-aligned more than 5 nm away from the BZO while several dislocations in YBCO lattice can be observed closer than that [25].

2 Experimental details

"What we observe is not nature itself, but nature exposed to our mode of questioning."
–Werner Heisenberg

2.1 Pulsed laser deposition of the superconducting thin films

2.1.1 Target synthesis

The microcrystalline (μ-) YBCO powders for the pulsed laser deposition (PLD) targets in [**P1**]–[**P3**] were prepared by solid state reaction, described in [78–82]. The nanocrystalline (n-) YBCO and $BaZrO_3$-doped (BZO-) n-crystalline YBCO targets in [**P4**]–[**P6**] were prepared by the citrate-gel method, described in [83, 84].

The Pr-doped YBCO targets in [**P1**]–[**P2**] were prepared using Y and Cu oxides, and Ba and Pr carbonates, each of 99.99% purity, resulting in powders of $Y_{1-x}Pr_xBa_2Cu_3O_{7-\delta}$ with $x = 0 - 0.20$, which were then pressed and sintered to form targets.

In [**P3**], the PLD targets were synthesized in two steps; YBCO and $BaCeO_3$ (BCO) were synthesized separately. The superconducting YBCO powder was prepared by solid state reaction using Y_2O_3, $BaCO_3$ and CuO powders of 99.99% purity. Proportioned powders were mixed, calcinated and sintered as described in [**P3**]. The $BaCeO_3$ powder was prepared by mixing $BaCO_3$ with CeO_2 of 99.99% purity and calcinated at 1200°C for 12h. Finally, the $BaCeO_3$ powder was mixed by 0, 2, 4, 6, 8 and 10 weight % into the YBCO powder, pressed into the form of targets and sintered at 910°C for 24 hours.

2.1.2 Deposition process

All the samples in [**P1**]–[**P6**] were pulsed laser deposited (PLD) thin films. Figure 11 shows a schematic description of the process. The pressure in the chamber was 300 mTorr of flowing O_2 during the ablation, and the XeCl-laser beam ($\lambda = 308$ nm) was focused to gain an energy density of ≈ 1.9 J/cm^2. The target was rotated to keep the plasma plume constant during the entire ablation. The on-axis geometry was used and the pressure (300 mTorr) together with the laser energy density was calibrated so that the tip of the plume just reached the substrate. The laser frequency was 5 Hz in all the samples and with these, optimized, parameters the film growth rate was 1 Å per pulse.

$SrTiO_3$ (STO) (100) single crystal substrates were used for film growth in [**P1**] and [**P3**]–[**P6**], MgO (100) single crystals were used in [**P2**], and technical substrates,

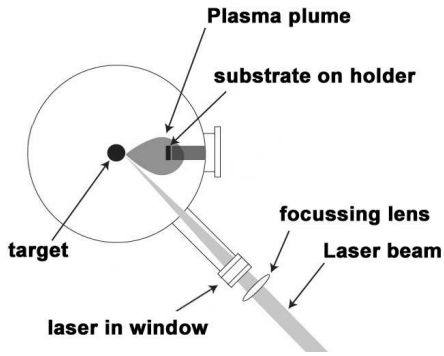

Figure 11. Schematic picture of the pulsed laser ablation setup.

Table 2. Lattice constants for the used substrates [85] and the mismatch to a- and b-axis of YBCO. All the materials are cubic.

	$SrTiO_3$	MgO	CeO_2/NiW
Lattice constant (nm)	3.905	4.213	5.411
Lattice mismatch (%)	1.2	9.1	-0.9

high-quality biaxially textured 5at.% W-doped Ni (NiW) tape with chemical solution deposited (CSD) $La_2Zr_2O_7$ (LZO) and CeO_2 buffer layer stacks, provided by Zenergy Power GmbH, were used in [**P2**] and [**P6**]. The lattice constants of the substrates and the mismatch to YBCO are presented in table 2. The lattice mismatch is calculated with the average of the orthorhombic YBCO's a- and b-axis. For CeO_2, the growth of YBCO is 45° rotated in-plane, which has been taken into account with a factor of $\sqrt{2}$. Figure 12 shows an illustration of the buffered NiW and single crystal STO substrates, the principle for the thin film structure on MgO single crystal substrate is identical with the illustration for STO in figure 12b.

The substrate temperature, T_s, during the deposition was optimized separately for all the substrates and targets. The most important optimization parameters were T_c, J_c and phase purity. However, the T_s was between 700°C and 750°C for all the samples, e.g. 750°C for samples in [**P3**]–[**P5**] and 725°C for samples on MgO and 700°C for samples on NiW in [**P2**]. T_s was measured with a thermocouple which was placed inside the substrate holder. The substrate was attached to the holder with silver paste for uniform heat conduction to the substrate and due to the slenderness of the buffered NiW substrate

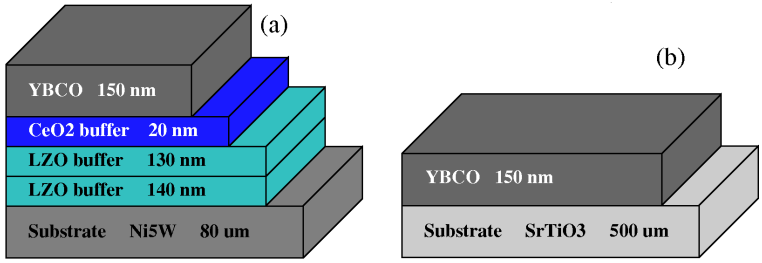

Figure 12. Illustrations of a) the high quality biaxially textured 5at.% W-doped Ni (NiW) tape with chemical solution deposited (CSD) $La_2Zr_2O_7$ (LZO) and CeO_2 buffer layer stacks, provided by Zenergy Power GmbH, and b) the $SrTiO_3$ (001) single crystal substrates with 150 nm of YBCO deposited.

(80 μm), it was first attached with silver paint on top of a single crystal MgO substrate. After the ablation, 1 atm of O_2 was applied after the temperature was decreased by 50°C for STO and MgO and 25°C for NiW with 10°C/min. After the O_2 was applied, T_s was kept the same for 10 minutes to achieve good oxygenation. The sample was then cooled with 25°C/min down to room temperature.

2.2 Photolithography

In order to determine the thickness of the films and to perform the current transport measurements, thin films were chemically etched in clean room facilities. The patterning was made by photolithography, where the desired pattern was exposed through a mask to the Megaposit SPRT 4180 M positive photoresist, which had been spinned into a thin layer on top of the film. The exposed photoresist was removed with diluted sodium hydroxide (NaOH), which does not react with non-exposed photoresist and YBCO. Finally, the pattern was etched to the YBCO film with diluted phosphoric acid (H_3PO_4) and the rest of the photoresist was removed with acetone.

2.3 Atomic force microscopy

Structural analysis with atomic force microscopy (AFM) was made with a ParkScientific AutoProbe AFM/STM/EFM/MFM system at room temperature and in air, to determine surface roughness, grain size and thickness of the sample, as well as to verify that the chemically patterned samples were undamaged and to measure the width of the stripes. Figure 13 presents a typical scan over a patterned stripe, with thickness of

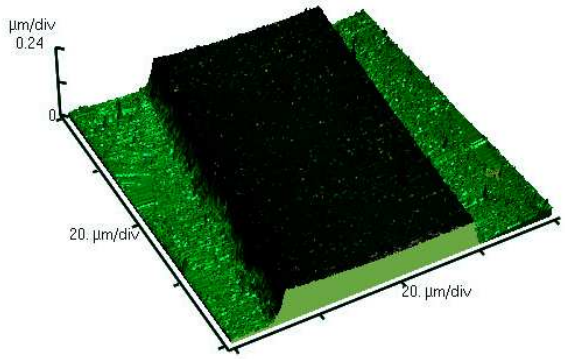

Figure 13. 80μm x 80μm AFM scan over a chemically etched stripe with dimensions of 45 μm x 150 nm. Colors are for an illustration.

180 nm and width of 45 μm. Cantilevers were Anfatec's triangular contact Si-tips with reflective coating. All the measurements were made in contact mode, which means that the tip of the cantilever touches the surface of the sample. The tip is swept on the sample with a given frequency and force. All the surface roughnesses are given in root-mean-square-(rms)-roughnesses.

2.4 X-ray diffraction

The X-ray diffraction (XRD) measurements of films were made using a Philips X'Pert Pro diffractometer with a Schultz texture goniometer. The used radiation was CuKα. The goniometer allows measurements in the usual 2θ direction, sample rotation ϕ and tilt angles ψ, as figure 14 shows. In the incident beam optics, a Ni filter was used to reduce the characteristic CuKβ-peaks and a 0.04 rad Soller slit with cups large enough so that the entire film surface was exposed. In the diffracted beam path a 0.18° entrance slit and a 0.04 rad Soller slit were used. In general, typical steps in each direction were 0.025° for 2θ, 0.1° for ϕ and 3° for ψ.

The phase purity of the thin film samples was measured with 2θ-scans perpendicular to film plane ($\psi = 0°$). Also, the full width at half maximum (FWHM) of the YBCO (005) was measured to investigate the structural quality in the c-axis direction. The out-of-plane crystallographic texture of the YBCO is determined by measuring the ω-scans from the YBCO (005) (rocking curves). The texture of the film and the ratio between the a- and c-axis oriented YBCO grains were measured from the YBCO (102) peak. The twin structure was determined from the YBCO (212)/(122) peaks at

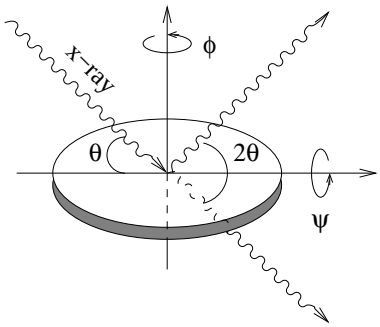

Figure 14. XRD's sample goniometer Bragg-angle 2θ, sample rotation ϕ and tilt angles ψ.

$(2\theta, \phi, \psi) = (56°, 26.5°, 73°)$, as they split into a four-peak set in the case of normal biaxial twinning. Also, FWHM (2θ, ϕ) of the YBCO (212)/(122) peaks were measured in [**P2**] to determine the average misorientation angle between the low-angle grain boundaries (GB's) (in ϕ), because the low-angle GB's broaden the YBCO (212)/(122) peak set [86], and to estimate the correlation between the strain and the Pr concentration (from the widening in 2θ). The lattice parameter c was determined from the difference of the YBCO (004), (005) and (007) peaks (or combination from these peaks) in the 2θ-scan with the Bragg equation

$$2d \sin 2\theta = n\lambda, \tag{12}$$

where d is the spacing of the planes ($d = c/l$ in the case of (00l) peaks), θ is the Bragg-angle, n is the order of the reflection and $\lambda = 1.54178$ Å is the wavelength for CuKα. The relative positions of the peaks were used to avoid the zero-point error. Because the dependency between c and the oxygen content is complex in YBCO thin films [87], the oxygen content of the lattice was determined from the intensity ratios between YBCO (005)/(004). When YBCO (005)/(004) intensity ratio is below 20, δ is between $0 < \delta < 0.3$ [87]. In BZO- and BCO-doped films, the structure and amount of dopant was investigated for BZO with (110) peak at $2\theta = 30.8°$ and for BCO with (004) at $2\theta = 41°$. For the BCO-doped samples, the (110) peak was not measured due to overlap with other peaks. In [**P3**] the average BCO-particle size was estimated with the Scherrer formula [88]

$$D_R = \frac{0.9\lambda}{b\cos(\theta)}, \tag{13}$$

where λ is the used x-ray wavelength, θ is the Bragg angle and b is the FWHM of the peak, expressed as $b^2 = b^2$(sample)$-b^2$(instrument).

The long range ordering, which is the distance over which atomic positions are correlated can be calculated from the lattice coherence length [89],

$$r_c = \frac{1}{\pi} \cdot \frac{c}{l\Delta\omega}, \tag{14}$$

where c is the lattice parameter, l is the order of the Bragg reflection and $\Delta\omega$ is the FWHM of the rocking curve.

2.5 Magnetometric measurements

The superconducting properties of the films were determined with magnetisation measurements which were made with Quantum Design's Physical Properties Measurement System (PPMS). In magnetometric measurements, the external field was applied parallel to the sample's c-axis and perpendicular to the film plane. T_c's were defined from the onset of the ac-magnetisation and the width of the transition was determined either as the difference between the onset and the temperature where 90% of the saturation is reached or as the difference between 10% and 90% of saturation. Hysteresis loops were measured by dc-magnetization at 10 K - 80 K in fields between -8 T and 8 T. J_c's were calculated using the Bean model for rectangular samples (equation 3).

In dc-magnetization measurements, the sample is magnetized by a constant magnetic field. It determines the equilibrium value of the magnetization in a sample, as the sample moment is constant during a single measurement. In the PPMS, the magnetic moment of a sample is measured by induction, producing a dc-magnetization curve $M(B)$, where M is the magnetization and B is the applied magnetic field. The ac-measurements obtain information about the magnetization dynamics, which dc-measurements do not yield. In ac-measurements, a small ac-drive magnetic field is superimposed on the dc-field, causing a time-dependent moment in the sample. The quantity of interest in ac-measurements is the dynamic susceptibility $\chi = dM/dB$, which is the slope of the $M(B)$ curve. In our ac-measurements the frequency was 113 Hz, which is not commensurable with 50 Hz of mains current and ac-field of 1 mT was applied without any external dc-field.

2.6 Electrical transport measurements

2.6.1 Measurements with PPMS

The critical current density measurements in [**P4**] were made with the PPMS in the maximum Lorentz force configuration ($B \perp I$) with the standard four probe method.

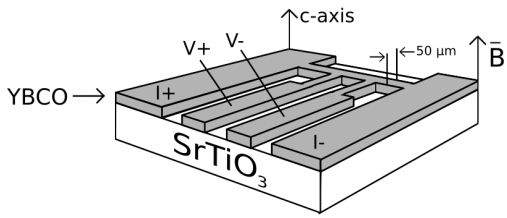

Figure 15. A schematic drawing of the experimental setup in the critical current measurements in pulsed magnetic field measurements [**P5**]. The contact pads for current ($I\pm$) and voltage $V\pm$, external magnetic field B and c-axis are illustrated for a sample which transport stripe is 50 μm wide. In BCO-doped samples and [**P4**] the angle, θ, between B and c-axis was varied in such, that $B \perp I$ always.

Contacts were made by sputtering either 50 nm of Au or a combination of Au and Ag on the patterned thin film contact pads and soldering Cu-wires with In. Soldering was done either at a low temperature ($\approx 250°$C) or by tapping at room temperature. Figure 15 presents a schematic drawing of the film pattern used in [**P4**]–[**P5**]. However, in BCO-doped samples and [**P4**] the horizontal rotator was used to measure the $J_c(\theta)$ curves, and therefore the angle between external field B and sample c-axis varied, while measurement current I was always perpendicular to B. The angle was varied with 2° steps and the critical current was defined with 10 μV/cm. Angular dependencies were measured between 10 K and 80 K in fields of 0.5 T and 1–8 T with 1 T steps.

2.6.2 Measurements with pulse magnet setup

In [**P5**], transport measurements were also made using the maximum Lorentz force configuration and standard four probe method, as shown in figure 15. An in-house built pulsed magnetic field system was used. The field pulse duration was 8 ms and during the field pulses, the resistivity $\rho(B)$ of the film samples were measured at 65, 70, 77, 85 and 88 K with transport currents up to I =100 mA, which represents 1.4 MA/cm^2 in the samples. Because the irreversibility field is above the achievable 30 T at 60 K, the measurements were limited to > 65 K.

3 Results and discussion

"Science is wonderfully equipped to answer the question "How?" but it gets terribly confused when you ask the question "Why?""
–Erwin Chargaff

3.1 Structural results

3.1.1 Surface roughness

Surface roughnesses were measured with AFM and the rms-roughness was typically determined as an average from three randomly selected (5x5)μm^2 or (10x10)μm^2 scans. As table 3 indicates, the surface rms-roughness in BCO-doped YBCO samples on STO [**P3**] remained below 8 nm in all samples without any correlation with the BCO concentration. Nevertheless, in the BCO-doped films the microstructure evolved with increasing dopant concentration, as figure 16 presents. The film surface grain size in the undoped sample is typical for what we observe with AFM, but already with 4 wt% of BCO, smaller grains appear, and this progress continues up to 10 wt% of BCO, where the surface grain size is highly irregular, compared with the undoped sample. This observation goes well with the apparent distribution of the BCO particles, observed with XRD, as we will discuss in paragraph 3.1.3. Also, the BCO's influence on the microstructure already at 5 wt% of doping has been observed earlier in bulk samples [20], where BCO refines the Y211 phase and was found to agglomerate and coarsen in both bulk and melt-textured samples [19, 20]. However, due to the method of calculating the surface roughness, there is no correlation between these observations. On the other hand, in BZO-doped samples on STO and NiW [**P6**] moderate BZO doping (< 5 wt%) was found to decrease surface roughness roughly by half on both substrates, e.g. for BZO-doped YBCO on STO the surface roughness decreased from 6.5 to 3.5 nm when BZO concentration increased from 0 to 4 wt%, respectively [90]. This correlation with BZO and surface roughness can be explained by a mechanism where BZO induces a change from 3D spiral growth to 2D type growth, leading to a very smooth surface [91]. This transition from spiral growth to two-dimensional nucleation and growth typically occurs if the surface mobility is increased [92].

In $Y_{1-x}Pr_xBCO$ ($x = 0 - 0.20$) thin films on MgO substrate [**P2**], the surface roughness remained around 10 nm up to 10% of Pr dopant without correlation to Pr concentration, but in the 20% doped sample, the roughness increased to 23.9 nm, as can be seen from table 3. This increase is caused by a large number of droplets on the

Table 3. Surface rms-roughness for BCO- and Pr-doped YBCO thin films measured with AFM.

BCO-doped (wt%)	0	2	4	6	8	10	
Roughness (nm)	5	5	8	6	3	6	
Pr-doped (x)	0.00	0.02	0.04	0.06	0.08	0.10	0.20
MgO Roughness (nm)	10.0	10.5	10.2	9.3	6.5	10.7	23.9
NiW Roughness (nm)	9.8	17.1	17.9	17.9	12.2	16.1	22.1

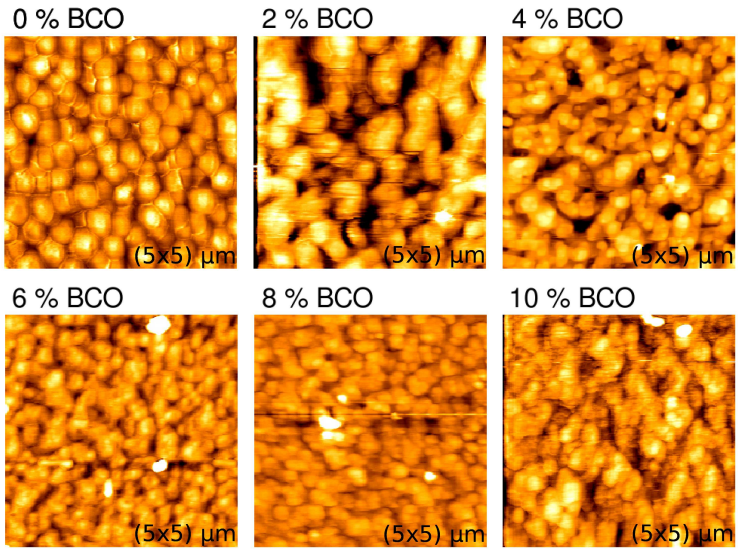

Figure 16. (5x5) μm AFM-scans from all the BCO-doped samples. The evolution of the microstructure goes from regular (0 % BCO) grain size towards irregular grain size, already visible at 4 wt% BCO-doped sample. However, surface roughness does not evolve with doping.

surface of the 20% doped sample. These values are essentially the same as in Pr-doped films on STO [**P1**] ($\simeq$10 nm), where no correlation was detected between the roughness and the Pr concentration. In contrast, in Pr-doped samples on buffered NiW substrate [**P2**], the surface roughness increases from 9.8 nm in the undoped sample to 17.1 nm in the 2% doped sample and the value remains roughly the same up to the 20% doped sample, as table 3 presents. In general, technical substrate always produces a rougher surface than STO or MgO, because the buffer layers of NiW substrate have surface roughness of 4.2 nm, whereas in single crystal STO and MgO the surface roughness is typically < 1 nm. On both substrates, the surface roughness of 8% doped sample is smaller than the trend implies, which is caused by the smaller number of droplets on the surface. However, in Pr-doped samples on MgO and on NiW, the surface roughness was approximately $2 - 4$ nm in the (2x2) μm^2 scans measured from the areas between the droplets, without correlation to Pr concentration. Even though the amount and size of droplets may indicate that the deposition parameters are not entirely optimized, one must take into account that every optimization process in these works were made with J_{c}, T_{c} and phase purity as the most important parameters.

3.1.2 Phase purity and grain orientation

The phase purity of the samples was measured with 2θ-scans in the range of 20° – 70° or 20° – 80°. As the results indicate, all the thin film samples were free from impurities and unintended additional phases. The figures 17 and 18 present the 2θ-scans for Pr-doped YBCO on MgO [**P2**] and BCO-doped YBCO on STO [**P3**], respectively, where nominal substrate and YBCO (00l) peaks are labelled. It is evident that in Pr-doped samples (figure 17) there is no notable effect on the crystal structure by the Pr-doping below 30% in YBCO [93, 94]. However, for BCO- and BZO-doped samples the dopant peaks are observed as they are additional phases.

In addition, all the films were c-axis oriented and the amount of a-axis oriented material was less than 2% and did not depend on dopant contents. Also, in samples on MgO substrate [**P2**], the amount of the 45° in-plane rotated grains was below 5% in all samples.

3.1.3 Dopants

In figure 18, a very wide peak around the expected BCO (004) peak at 41° (arrow) indicates that BCO is distributed into the lattice as very small particles in (00l) orientation. The average BCO particle size is estimated from the Scherrer formula (equation 13) to

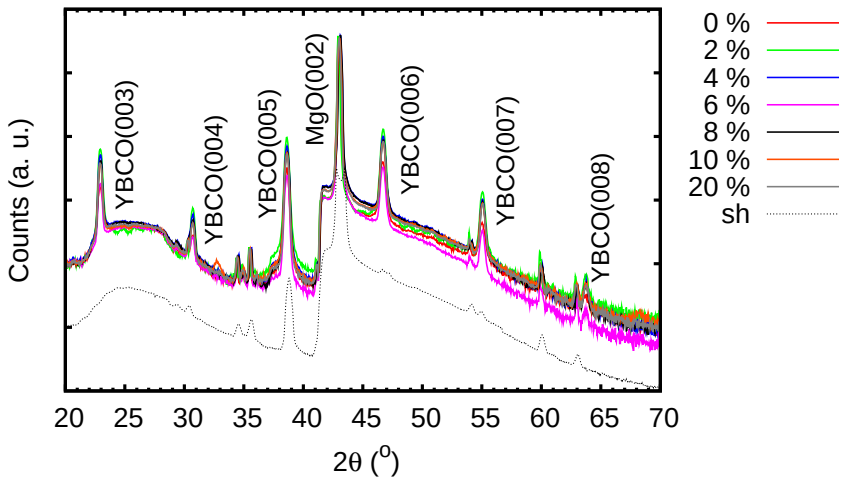

Figure 17. 2θ-scans show YBCO (00l) peaks without impurities for $Y_{1-x}Pr_xBCO$ samples on MgO. The signal from the substrate and sampleholder (both MgO) is shown as curve "sh". Intensities (counts) are in logarithmic scale.

be around 2 nm. Due to this size distribution of the BCO in the lattice, no nominal BCO (004), (110) nor their rocking curves could be measured.

For BZO-doped samples [**P5**]–[**P6**] the BZO (110) peak intensities increase almost linearly with dopant concentration. Texture measurements show that BZO grows cube-on-cube with YBCO on both STO and NiW substrates, and according to earlier measurements, the BZO forms a network of correlated nanorods aligned along the YBCO c-axis on both STO and NiW substrates [25, 95]. The in-plane texture analysis for BZO-doped samples [**P5**]–[**P6**] shows that all the films are textured in the ab-plane, except the 9 wt% BZO-doped sample, where 3 – 5wt% of the material is rotated in-plane by 45° from the substrate (100) direction in samples on both substrates. In YBCO films on NiW substrates ([**P2**] and [**P6**]) the peaks are very broad in ϕ, without correlation to the BZO content [**P6**]. This is related to a large number of low-angle grain boundaries and in-plane spread of the YBCO grains [96, 97].

3.1.4 Low-angle grain boundaries

In Pr-doped YBCO thin films on MgO and NiW [**P2**], the average in-plane misorientation angle between the grains (labelled as "GB angle" in table 4), estimated from FWHM-ϕ of the (212)/(122) peak set, correlates with the Pr concentration. In samples

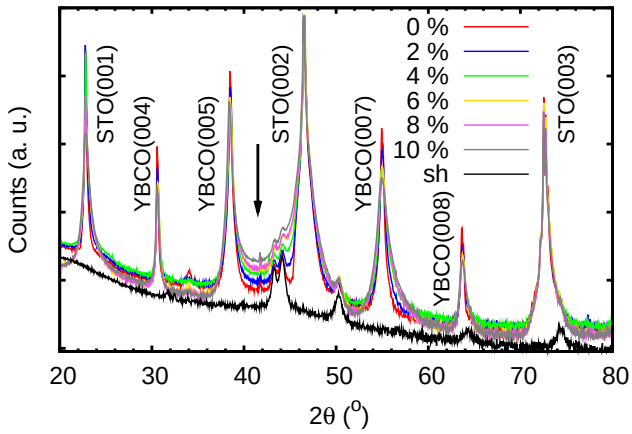

Figure 18. 2θ-scans show YBCO (00l) peaks without impurities and a very wide peak (arrow) at 41°, FWHM $\simeq$ 5°, increasing with BCO content. The signal from the sampleholder is shown as curve "sh". Intensities (counts) are in logarithmic scale.

on MgO, the GB angle increases from the 2% Pr-doped sample ($\simeq$1.6°) up to the 6% doped sample ($\simeq$2.2°). Above that the GB angle decreases with increasing Pr concentration, but remains larger than in the undoped sample up to the 20% doped sample. In YBCO thin films on MgO, GB's exist due to lattice mismatch, as presented in table 2. This have been also observed earlier with TEM [97]. The GB angle is larger in all the Pr-doped samples (excluding 2%-doped on MgO where the value is practically the same), compared with the undoped sample. This can be explained by Pr induced variation in the structural expansion of the dislocation cores in the GB's, as reported for Ca^{2+} [98], but a more specific explanation cannot be made from XRD data. In samples on buffered NiW, the GB angle varies between 3.5° and 4.8°, which is slightly less than the average misorientation angle $\simeq$ 5°, measured from the pure substrate. In PLD thin films ($<$ 500 nm) GB's do not meander and the GB network imitates nearly directly the substrates GB's [99]. Therefore, in samples on NiW, GB's exist despite the negligible lattice mismatch between CeO_2 and YBCO, as presented in table 2.

3.1.5 c-axis lattice parameter

The determined YBCO c-axis lattice parameter (equation 12) in Pr-doped samples on MgO [**P2**] (table 4) was found to decrease to 1.163 nm with 8% or Pr from the nominal 1.168 nm [31], whereas it increases up to $\simeq$1.166 nm at 10% and 20% doped samples,

Table 4. Selected structural properties measured with XRD for all $Y_{1-x}Pr_xBCO$ (x = 0 - 0.20) on both MgO and buffered NiW substrates and for BCO-doped YBCO thin films on STO.

$Y_{1-x}Pr_x$BCO/MgO							
x	0.00	0.02	0.04	0.06	0.08	0.10	0.20
GB angle (°)	1.58	1.57	1.68	2.19	1.99	1.96	1.83
c-axis (nm)	1.168	1.168	1.166	1.165	1.163	1.167	1.166
$I(005)/I(004)$	16.16	14.29	14.62	13.92	16.60	16.87	16.01
FWHM (005) (°)	0.360	0.332	0.338	0.344	0.343	0.337	0.314
FWHM ω (005) (°)	0.643	0.441	0.374	0.685	0.390	0.371	0.398
r_c (nm)	6.6	9.7	11.4	6.2	10.9	11.5	10.7
$Y_{1-x}Pr_x$BCO/NiW							
x	0.00	0.02	0.04	0.06	0.08	0.10	0.20
GB angle (°)	3.54	3.84	3.87	3.63	3.99	4.30	4.71
c-axis (nm)	1.168	1.168	1.169	1.168	1.168	1.168	1.168
$I(005)/I(004)$	12.19	11.14	10.45	12.10	12.64	11.41	13.15
FWHM (005) (°)	0.374	0.379	0.378	0.326	0.367	0.381	0.345
FWHM ω (005) (°)	6.387	4.543	5.492	5.650	5.770	5.463	5.385
r_c (nm)	0.7	0.9	0.8	0.8	0.7	0.8	0.8
BCO+YBCO/STO							
Sample	0 wt%	2 wt%	4 wt%	6 wt%	8 wt%	10 wt%	
c-axis (nm)	1.168	1.167	1.164	1.165	1.165	1.168	
$I(005)/I(004)$	13.70	14.68	18.08	18.80	14.40	19.40	
FWHM (005) (°)	0.1578	0.1997	0.2358	0.2473	0.3643	0.2405	
FWHM ω (005) (°)	0.2840	0.3210	0.4212	0.4300	0.3495	0.4757	
r_c (nm)	15.0	13.3	10.1	9.9	12.2	9.0	

indicating a small increase in the distorting effect up to the 8% Pr concentration. In samples on NiW [**P2**] c stays practically the same, which can be a consequence of a more relaxed lattice in samples on NiW than in those on MgO, as the 2θ-FWHM's of the YBCO (212)/(122) peak set are 10% smaller in samples on NiW than in samples on MgO, indicating less strain and a more relaxed lattice.

For μ-crystalline bulk samples, c has been found to increase when Pr substitutes Y, and to decrease when Pr substitutes Ba [15,100]. The decrease in the c parameter values in Pr-doped samples on MgO indicates that Pr can also substitute the Ba site, which is possible in the GB regions, because in the GB regions under compression and tension, Ca has been reported to replace also Ba- and Cu-sites, relieving strain and suppressing O vacancy formation [101]. Also, as already in the 5% Pr-doped YBCO (on the Ba site) T_{c} is below 50 K [100], it is evident that if this Ba substitution occurs, it takes place only in a very small fraction of the sample. Generally in thin films, larger a- and b-axes in the substrate than in the thin film cause strain which can decrease the c-axis of the thin film. Still, the correlation between c-axis parameter and Pr concentration in Pr-doped samples on MgO indicates that we have competing effects, but no comprehensive explanation can be made from this data. Though we cannot detect any change in the c parameter in the Pr-doped samples on NiW, it is still reasonable to expect that Pr substitutes both sites also in these samples. We cannot see this directly due to the excess amount of other lattice defects in the Pr-doped YBCO on this technical substrate.

For BCO-doped samples [**P3**] the c-axis decreases from the nominal value 1.168 nm [31] of the undoped sample to 1.164 nm of the 4 wt% sample, and increases back to the nominal value of the 10 wt% sample. In BZO-doped samples [**P6**] the c-axis increases slightly when BZO concentration increases. This can be explained with the BZO's larger lattice parameter ($a = 4.19$ Å) comparing with YBCO and the columnar defect network through the film, which produces the ordered structure of strains and dislocations [25]. Different correlations between c and dopant concentrations in BCO- and BZO-doped films can be explained by the smaller strain in BCO-doped samples, as observed in the next paragraph.

3.1.6 Twins

For BCO-doped samples the twinning was found to remain biaxial and visible up to 10 wt% of BCO, as seen in figure 19. In comparison with BZO doping, the YBCO (212)/(122) peaks cannot be separated from each other because of the lattice strain above 2.6 wt% of BZO [75]. Although the lattice parameter of BCO ($a = 4.40$ Å)

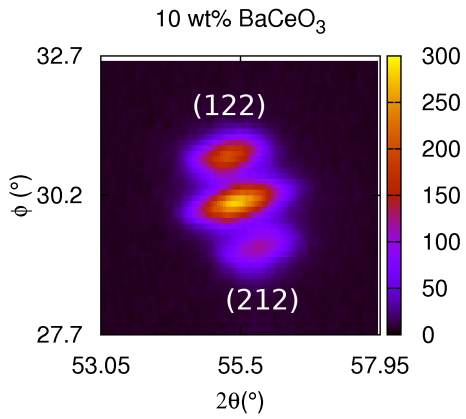

Figure 19. $(2\theta, \phi)$ scan of YBCO (212)/(122) peak set for 10 wt% BCO-doped sample on STO. Twinning was found to remain biaxial and visible up to 10 wt% of BCO. The wide peak in the center is the superposition of two peaks.

is larger than in BZO, it is evident that the strain is notably smaller in BCO-doped thin films and there is no columnar defect network. Therefore, the c-axis correlation is different between BCO and BZO. This result is in line with the earlier observation from the BCO (004) peak, showing that the BCO distribution in the YBCO lattice differs notably from the structure of the BZO in the thin films [25]. Nevertheless, an interesting feature was observed in BCO-doped samples, especially with the 6 wt% of BCO, but also with 4 wt% and 8 wt%. In this dopant range, three different twinning systems were observed, as shown in figure 20. From sample to sample, either biaxial (20a), uniaxial (20b) [102] or an additional direction of twins (20c) were found. Even though the normal biaxial one was the most common result, this result indicates a fairly chaotic growth process, despite of the similar ablation parameters between samples. Because the superconducting properties were notably decreased in uniaxial and "triaxial" samples, only the results from magnetic measurements with biaxial samples are presented in this work. The peak split in $(2\theta, \phi)$ scans of (212)/(122) could not be detected in samples on MgO and NiW, which is due to the presence of low angle GB's.

3.1.7 Oxygen content

The oxygen content of the lattice was near optimum in all samples, as the YBCO (005)/(004) intensity ratios were below 20 [87] in all samples (table 4). For Pr-doped

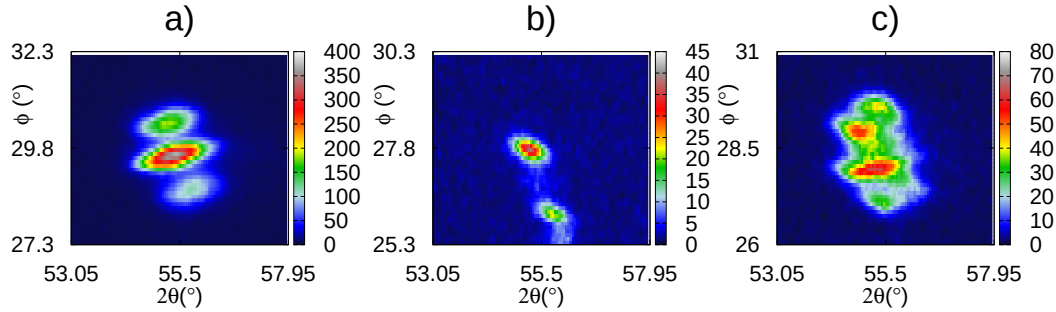

Figure 20. $(2\theta, \phi)$ scans of YBCO (212)/(122) peaks for three different 6 wt% BCO-doped samples on STO. BCO induces a somewhat chaotic growth process, leading to either biaxial (a) uniaxial (b) or biaxial with the additional direction of twins (c) twinning.

samples [**P1**]–[**P2**] this was expected, as it has been reported that Pr does not influence the oxygen content in $Y_{1-x}Pr_xBCO$ compounds [94, 103, 104]. Moreover, though heavier cationic substitution of Y site increases the (005)/(004) ratio [105], the values remain below 20 even with the 20% Pr-doped samples. For BZO-doped samples [**P6**] YBCO (005)/(004) was found to vary without correlation to BZO content between 13–15 for samples on STO and 9–14 for samples on NiW. In contrast, for BCO-doped samples [**P3**] the ratio increases with 4, 6 and 10 wt% samples, as table table 4 shows, indicating increasing oxygen deficiencies with increasing BCO concentration. However, the value remains below 20 and the 8 wt% doped sample presents an exception from this trend. This can be connected with the observed complex growth dynamics in 4–8 wt% BCO-doped samples, but it still implies that BCO induces more oxygen deficiencies than BZO into YBCO.

3.1.8 Peak widths

The FWHM of (005) peaks remain relatively small, close to the instrumental value, in Pr- and BZO-doped samples, as shown for Pr-doped samples in table 4, which indicates high structural quality in the c direction. For BCO-doped samples some increase can be detected with increasing dopant concentration, indicating a slight increase in the c-lattice parameter variation.

The long range ordering or the lattice coherence length r_c (equation 14) is smaller in undoped samples on MgO and NiW than in the samples on STO, and moreover, the

values for samples on NiW are extremely short which is caused by the strong mosaic spread of YBCO grown on NiW [106]. For undoped YBCO on STO r_c is in typical range 15–20 nm [**P6**] [107]. Pr-doped sample on MgO presents an interesting feature, where r_c increases with doping from 6.6 nm in the undoped sample to $\backsimeq$ 10 nm in the doped samples (excluding the 6% doped sample) indicating that Pr-doping decreases the amount of lattice distortion. For BCO- and BZO-doped samples the increasing dopant concentration decreases r_c, as expected and values are comparable with each other e.g. with a 9 wt% BZO-doped sample r_c is 12 nm [**P6**], which is close to the $r_c = 9.0$–12.2 nm for 10 wt% and 8 wt% BCO-doped samples (table 4).

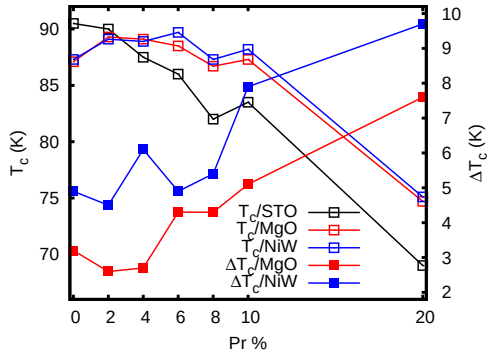

Figure 21. Dependence of the critical temperature T_c on Pr concentration for all the Pr-doped films [**P1**]–[**P2**] and the width of the magnetic transition ΔT_c for films grown on MgO and NiW substrates [**P2**]. For samples on STO [**P1**], ΔT_c was between 2.5–3.5 K and did not correlate with Pr concentration.

3.2 Superconducting properties

3.2.1 Critical temperature

The superconducting transition temperature, T_c, measured from the onset in the real part of ac-magnetization at 0 T was found to decrease almost linearly in Pr-doped samples on STO [**P1**], as shown in figure 21. However, in samples on MgO and NiW [**P2**] T_c increases in $2\% - 6\%$ Pr-doped samples from the undoped sample values and above 6% of Pr concentration the T_c's start to decrease (figure 21). The most narrow transitions are observed at 2% doped samples, as also seen in table 5. Decrease in T_c and increase in ΔT_c with higher Pr concentrations are caused by an increasing number of badly superconducting areas of PrBCO, as no impurities were detected in samples. While the correlation between T_c and Pr concentration is similar in samples on MgO and NiW, it differs from the Pr-doped bulk samples of YBCO [15] and single crystal samples on STO [**P1**], where T_c decreased with increasing Pr concentration.

The increase in T_c at low Pr concentrations for samples on MgO and NiW indicates that the intra-grain inhomogeneity of superconductivity does not increase until above 10% of Pr concentration samples. We propose that this is due to non-homogeneous distribution of Pr atoms in the lattice and it is possible that Pr segregates into the GB regions. As mentioned earlier, Ca^{2+} doping is well known to increase $J_c^{gb}(B)$ [16–18]. Song et al. [98] have also shown that Ca segregates near the dislocation cores (GB's). Moreover, Klie et al. [101] have shown that the ionic radius of the cationic substitute is

Table 5. Selected superconducting properties measured by magnetometry for all BZO- and BCO-doped YBCO thin films on STO and $Y_{1-x}Pr_xBCO$ (x = 0 - 0.20) on both MgO and buffered NiW substrates

BZO+n-YBCO/STO							
Sample	0 wt%	1 wt%	2.6 wt%	4 wt%	5 wt%	7.5 wt%	9 wt%
T_c(K)	90	90	90	88	88	87.5	86.5
BCO+YBCO/STO							
Sample	0 wt%	2 wt%	4 wt%	6 wt%	8 wt%	10 wt%	
T_c(K)	90.3	88.7	87.2	86.2	87.7	83.7	
ΔT_c(K)	1.9	2.0	5.5	5.4	5.9	6.7	
At 10 K							
J_c(0 T)(MA/cm^2)	42.9	43.2	28.6	22.8	18.8	15.7	
J_c(4 T)(MA/cm^2)	4.02	6.07	6.60	5.07	3.61	3.96	
$Y_{1-x}Pr_x$BCO/MgO							
x	0.00	0.02	0.04	0.06	0.08	0.10	0.20
T_c(K)	87.1	89.3	89.1	88.5	86.7	87.3	74.7
ΔT_c(K)	3.2	2.6	2.7	4.3	4.3	5.1	7.6
At 10 K							
J_c(0 T)(MA/cm^2)	42.2	45.8	43.7	37.1	21.6	19.9	14.9
J_c(4 T)(MA/cm^2)	10.2	7.75	6.85	6.65	2.88	2.91	1.54
At 77 K							
J_c(0 T)(MA/cm^2)	2.21	3.20	2.98	1.94	0.84	1.00	-
J_c(1 T)(MA/cm^2)	0.08	0.27	0.20	0.18	0.02	0.03	-
$Y_{1-x}Pr_x$BCO/NiW							
x	0.00	0.02	0.04	0.06	0.08	0.10	0.20
T_c(K)	87.3	89.1	88.9	89.7	87.3	88.2	75.1
ΔT_c(K)	4.9	4.5	6.1	4.9	5.4	7.9	9.7
At 10 K							
J_c(0 T)(MA/cm^2)	13.3	16.4	11.5	11.4	13.2	11.4	4.19
J_c(4 T)(MA/cm^2)	2.89	4.11	2.80	2.61	2.64	2.55	0.72
At 77 K							
J_c(0 T)(MA/cm^2)	1.30	1.82	1.13	1.07	0.85	0.80	-
J_c(1 T)(MA/cm^2)	0.01	0.14	0.07	0.03	0.01	0.03	-

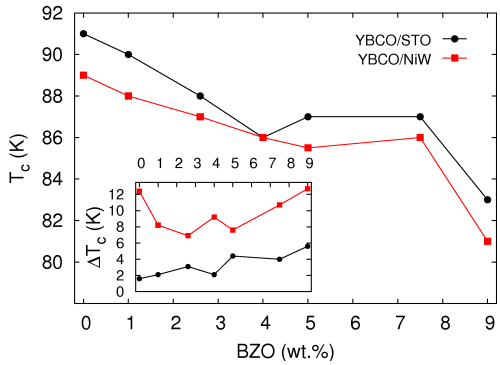

Figure 22. Dependence of the critical temperature T_c on BZO dopant concentration and the width of the magnetic transition ΔT_c (inset) for BZO+n-YBCO films grown on both STO and NiW substrates.

more important than the electronic valences for enhancing $J_c^{\mathrm{gb}}(B)$. Because the ionic radii of Ca^{2+} and Pr^{3+} are practically the same (100 pm for Ca^{2+} and 99 pm for Pr^{3+}) our hypothesis is plausible.

T_c was found to decrease with increasing dopant concentration with BCO [**P3**] and BZO [**P4**]–[**P6**], as presented in table 5 and figure 22, respectively. As shown in table 5, the values of T_c decrease from 90.3 K to 83.7 K as the BCO concentration rises to 10 wt%. At the same time, the width of the transition ΔT_c increases from 1.9 K to 6.7 K. This correlation is comparable with BZO-doped samples [**P5**] where T_c decreases from 90 K for 0–2.6 wt% to 86.5 K for 9 wt%, as table 5 shows. This can be explained by the increasing number of defects with increasing dopant concentration and the results are in line with earlier results [75]. For the μ-, n- and BZO+n films on STO [**P4**], T_c's were determined from resistivity measurements and the values were 91, 91 and 87 K respectively. It has been reported for BCO-doped YBCO samples that in metalorganic chemical vapour deposition (MOCVD) films T_c did not decrease [24]. This can be connected to the different structure and growth dynamics in MOCVD films compared with PLD thin films. As figure 22 presents, T_c decreases with increasing BZO content similarly on both substrates. However, the width of the transition ΔT_c is notably larger in samples on NiW ([**P2**] and [**P6**]), which can be connected to the excess amount of lattice defects and in-plane spread in samples on NiW. In samples on STO, ΔT_c increases almost linearly, indicating increasing distorting effect of BZO. In BZO-doped films the decrease in T_c is generally connected to the strain effect [108]. Because the strain is notably smaller in BCO-doped samples, as structural results indicate, the decrease in T_c

can be explained by large amount of lattice defects in the interface between YBCO and the BCO particles, as the lattice mismatch is relatively large ($\simeq 14\%$).

3.2.2 Critical current densities vs. dopant concentration

Our earlier results on sintered bulk samples showed significantly increased J_c in Pr-doped YBCO samples [15]. However, as figure 23 presents, Pr-doped thin film samples on STO [**P1**] show suppression of J_c with increasing Pr content in all measured fields and temperatures. Although PLD optimization was also done with the 8% Pr-doped samples, as this Pr concentration gave the highest J_c in bulk samples [15], the undoped sample had the highest J_c in the whole field and temperature range in samples on STO. On the other hand, in Pr-doped samples on MgO and NiW [**P2**] J_c increased in low dopant concentrations ($\leq 4\%$), as seen in figures 24–25 and in table 5 where J_c(0 T and 4 T, 10K) and J_c(0 T and 1 T, 77 K) are presented. In samples on MgO, J_c increased for 2% of Pr in self-field (0 T) and in all fields at temperatures $\geq$ 60 K, as figures 24a and 25a present. J_c increased for 2% of Pr on NiW at all fields and temperatures, and the relative increase is larger in higher fields, as shown in figures 24b and 25b. On both substrates (MgO and NiW) where J_c increased with Pr-doping compared with the undoped sample, the increase is the largest with 2% of Pr-doping. Because in multicrystalline samples and e.g. coated conductors, J_c is perniciously determined by GB's [39, 109–111], it is evident that J_c^{gb} is the largest limiting parameter of J_c in undoped samples on MgO and NiW. However, in samples on STO, due to the low lattice mismatch between STO and YBCO, GB's are not present, and therefore only decreasing SC properties are observed with increasing Pr concentration. In general, J_c's decrease exponentially when the misorientation angle exceeds 2°-7° [112] and above 10° GB's show Josephson-like behaviour, which causes a weak coupling where the $J_c^{gb}(B)$ decreases rapidly. The possible explanation for the J_c increase on Pr concentration in samples on MgO, only in the self-field and temperatures above 60 K, can be connected to the increased T_c, where the effect of Pr is emphasized at higher temperatures. In samples on NiW, J_c is more limited by the GB's than in samples on MgO, due to the larger number of GB's and larger GB angles (table 4), therefore the effect is observed at all the temperatures. Results (figures 23–25) also indicate that there might be some problem with the 8% Pr-doped target, because J_c values for 8% doped films are low, especially at high temperatures. However, no impurities nor change in the target density were observed.

In BCO-doped YBCO thin films [**P3**] J_c was found to increase with low dopant

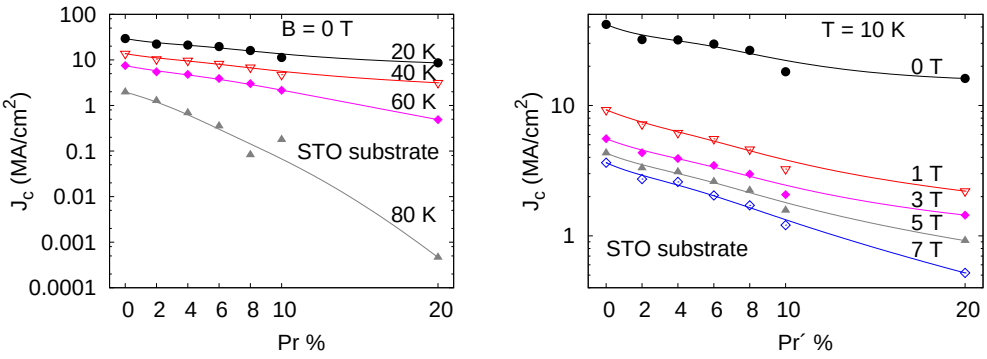

Figure 23. a) J_c for all the $Y_{1-x}Pr_xBCO$ film samples on STO in $B = 0$ T at different temperatures and b) at 10 K in different external fields. Lines are for guiding the eye.

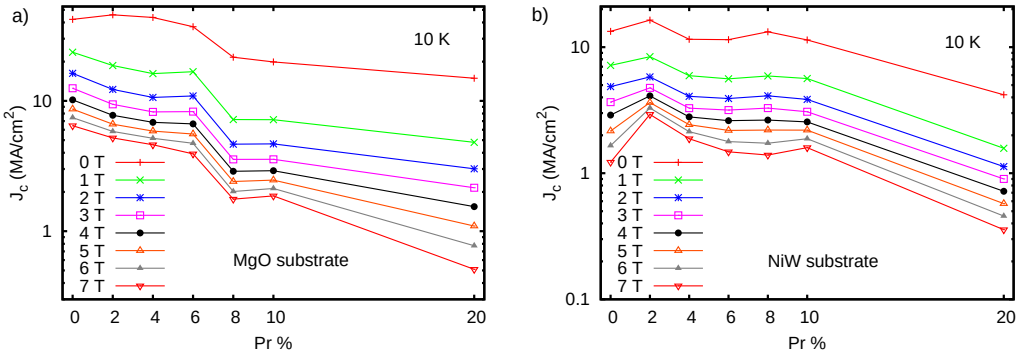

Figure 24. J_c for all the Pr-doped samples on a) MgO substrate and on b) buffered NiW substrate at 10 K in all the measured external fields. a) The Pr-doping does not increase J_c on MgO substrate in the presence of the external field at 10 K; only the self-field J_c(0 T) is slightly increased at the 2% Pr-doped sample. b) On buffered NiW substrate the Pr-doping increases J_c in all fields and the relative increase is larger in higher fields. The largest increase happens in the 2% Pr-doped sample, and above 4 T, also the 4% doped sample's J_c is larger than in the undoped sample.

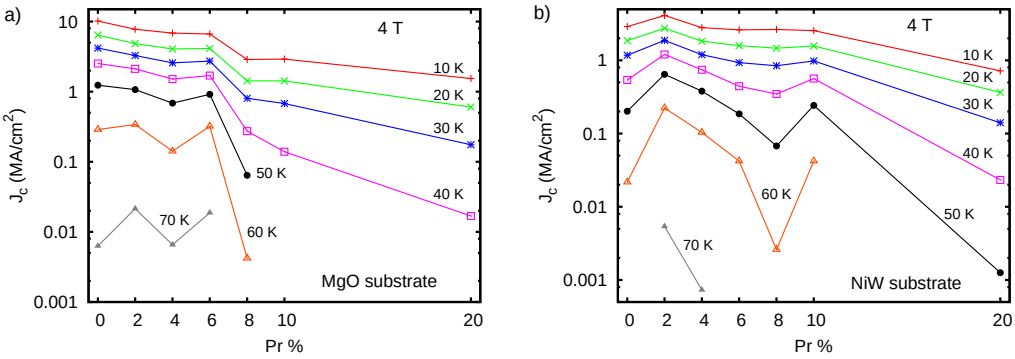

Figure 25. J_c for all the Pr-doped samples on a) MgO and on b) buffered NiW substrate in the external field of 4 T. a) J_c increases with Pr-dopant at 60 K and above. This behaviour is consistent in all the measured fields in samples grown on MgO substrate. b) On buffered NiW substrate, the J_c increases in all the measured temperatures and the relative increase is larger at higher temperatures. The largest increase takes place at the 2% Pr-doped sample. All the samples were above B_{irr} at 80 K in 4 T.

concentration in certain conditions. While the self-field J_c decreases with increasing BCO-doping, J_c increases notably in the high-field region, having a maximum around BCO 2-4 wt%, as can be concluded from figure 26. It is noteworthy that the optimal dopant concentration, n_{opt} shifts from 4 wt% to 2 wt% as the temperature rises above 30 K and the field rises above 3 T, as can be seen in figure 26a. The improvement in J_c is also field dependent, as can be seen in figure 26b, where the increase in J_c occurs only in the presence of an external magnetic field.

The temperature dependencies of J_c in self-field and in 3 T for BZO+n-films on STO and NiW [**P6**] are shown in figure 27. In films on STO (0 T) (figure 27a), optimal doping concentration of 2.6–4 wt% produces the highest J_c's below 80 K, as observed also earlier [75]. In the field range $B > 3$ T, n_{opt} increases slightly, as shown in the inset of figure 27a. In low field range, the 9 wt% of BZO is clearly the weakest but in fields above 3 T its J_c is higher than that with BZO content less than 1 wt%.

In samples on NiW, n_{opt} is higher than for samples on STO. The value of n_{opt} increases to 7.5 wt% in samples on NiW in the whole measured field and temperature range, as figure 27b shows. However, J_c in the 9 wt% doped sample is clearly smaller, which can be connected to the structural results. In 9 wt% BZO-doped samples $45°$ in-plane rotated material causes weak links, which reduce J_c. Earlier results from n-

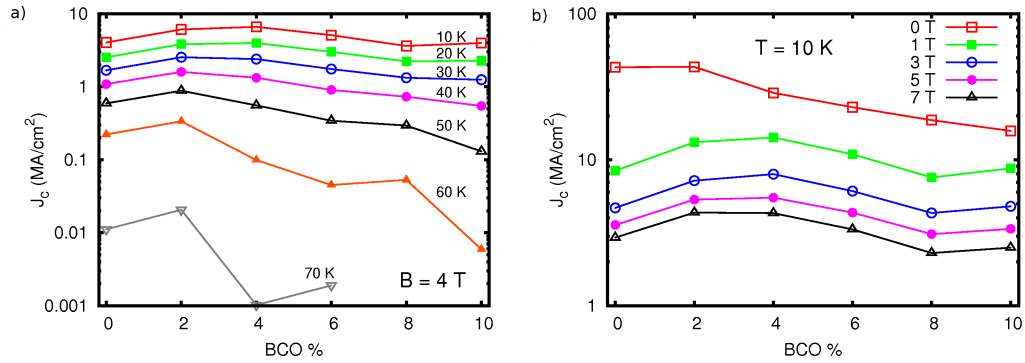

Figure 26. J_c for all BCO-doped samples a) in the external field of 4 T and b) at 10 K for selected external field values. a) The optimal dopant concentration, n_{opt} shifts from 4 wt% to 2 wt% as the temperature rises above 30 K and b) the improvement in J_c with the BCO doping is field dependent. Samples were above the irreversibility field B_{irr}, where $J_c = 0$, at 80 K in 4 T and likewise at 70 K for the 8 wt% and 10 wt% samples.

YBCO thin films show that n_{opt} is slightly higher ($\simeq$ 4 wt%) [25] than those reported on μ-YBCO thin films ($\simeq$ 2 wt%) [113,114]. This increase in n_{opt} is connected with the larger number of structural defects in samples ablated from n-grained targets. Therefore, higher n_{opt} in samples on NiW can be qualitatively explained by a higher defect density, which is in line with the structural results.

J_c increased for low dopant concentrations of Pr and BCO. For Pr, the presence of GB's seems to be necessary for increasing J_c, and therefore the effect of Pr is connected to J_c^{gb}. For BZO, n_{opt} was found to depend strongly on substrate and external field range.

3.2.3 Magnetic field dependence of J_c

In Pr-doped thin films on MgO and NiW at 77 K, the 2% Pr-doped samples J_c's were higher than in the undoped samples in the whole field range, as presented in figure 28. Also, the J_c of the 2% Pr-doped sample on NiW was higher than the undoped sample on MgO above 1 T. As observed, $J_c(B)$ dependence is different between samples on MgO and NiW. For samples on MgO, the shape is rounder (in double logarithmic plot) than in samples on NiW, where a clear plateau is observed in the low-field region. The round shape complicates the correct fitting of equation 8 and, therefore, the defined α values depend strongly on the end-point of fitting. This can also be associated to the flux

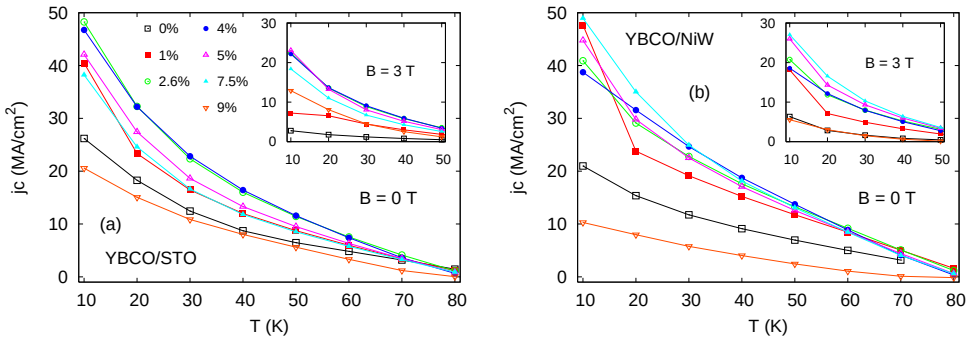

Figure 27. Temperature dependence of J_c (labelled as j_c) measured in fields of 0 T and 3 T (inset) for BZO-doped films deposited on STO (a) and NiW (b) substrates. The symbols in figure (b) correspond the same BZO concentrations than in (a).

creep [115] which leads to a round shape of the $J_c(B)$ curve. The shape, however, does not change with Pr, the curves are only shifted with different dopant concentrations. At low temperatures, samples on both substrates show a clear plateau at the low-field region and the $J_c(B)$ dependencies are similar, but at higher temperatures only the samples on NiW show a clear plateau in the low-field region. The shape of $J_c(B)$ of the NiW films at high fields were reported for films with columnar defects [75, 116–118]. Hence, GB's are the reasonable cause. However, on MgO, the shape of $J_c(B)$ curve is typical for an undoped YBCO sample grown on single crystal substrate (e.g. STO and MgO) for all the dopant concentrations. Nevertheless, this difference also affects B^* and α, as we will see later in this work, and this distinction is connected to the different amount of GB's or other defects, acting as pinning sites, but no comprehensive explanation has been made.

Figure 29 presents a comparison of the $J_c(B)$ behavior between undoped μ-YBCO, 4 wt% BCO- and 4 wt% BZO-doped (optimal doping [75]) YBCO samples at 10 K. The $J_c(B)$ curve of the BCO-doped sample is between the undoped and the optimally BZO-doped sample. This can be connected to the different pinning dynamics and the absence of columnar defects, as the structural results suggest for BCO-doped samples. The only measured temperature, 80 K, where BCO-doped sample gave higher J_c in the whole field range than optimally BZO-doped sample is shown in the inset of figure 29. Nevertheless, the J_c values of 2 wt% BCO-doped sample at 80 K are nearly the same as in the undoped sample, as well as in the other region where 2 wt% BCO-doped sample gave a higher J_c than the BZO-doped sample, in 0 T, from 40 K to 80 K. For BZO-doped

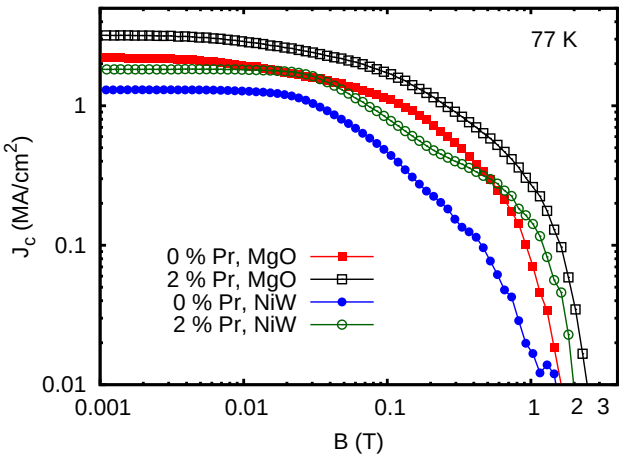

Figure 28. Magnetic field dependence of J_c measured at 77 K for the undoped and 2% Pr-doped samples for MgO- and NiW-substrate. At 77 K, the 2% Pr-doped samples have higher J_c in all the fields, compared with the undoped samples on both substrates.

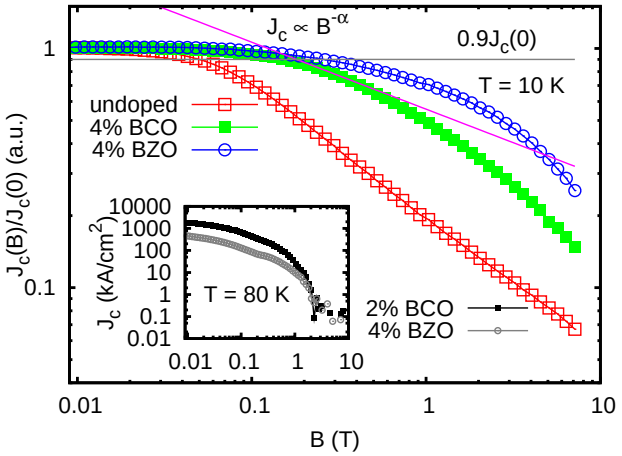

Figure 29. Definition of the accommodation field $B^* = 0.9J_c(0)$ and α, with the comparison of $J_c(B)$ at 10 K in undoped, 4 wt% BCO-doped and 4 wt% BZO-doped YBCO films on STO. Inset presents a comparison between 2 wt% BCO-doped and 4 wt% BZO-doped sample at 80 K.

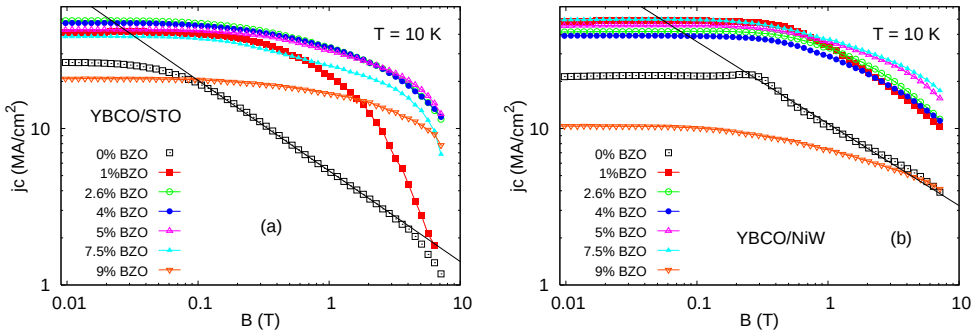

Figure 30. $J_c(B)$ curves measured at 10 K for BZO-doped films grown on STO (a) and NiW (b) substrates. The example of the fit (equation 8) to double logarithmic plot is shown in 0wt.% BZO data.

films on STO and NiW [**P6**], the $J_c(B)$ curves at 10 K are shown in figure 30. $J_c(B)$ curves for all the BZO+n-films at 10 K [**P5**], together with the determined B^* and α values are presented in figure 31. In BZO-doped samples on STO (figures 30a and 31), the shape of $J_c(B)$ changes with doping, as observed earlier [119,120]. The lengthening of the low-field plateau in BZO-doped samples is due to the increase in the density of strong pinning sites. Also, BZO creates substantially less field-dependent $J_c(B)$ curve on STO in the high-field region already with 2.6 wt% of BZO, as seen in figure 30a, and this can be explained by the effects of anisotropic flux pinning and vortex curvature [86]. The $J_c(B)$ shapes are similar between optimally doped samples $n_{opt} = 2.6$–4 wt% on STO and $n_{opt} = 5$–7.5 wt% on NiW (figure 30b). Still, the undoped sample on NiW presents a significant disparity. The undoped sample curve is typical for YBCO on NiW, as observed with the undoped sample on NiW in Pr-doped sample series (figure 28). The crossover where J_c starts to decrease with increasing B in samples on NiW is connected to the opacity of the GB network [121]. However, whereas the effect of Pr on the shape of the $J_c(B)$ was insignificant, in BZO-doped films on NiW already the 1 wt% doped sample shows the typical curvature for BZO-doped YBCO. This difference is obviously caused by entirely different doping mechanism.

Whereas the effect of Pr on the shape of $J_c(B)$ is almost negligible, both BCO and BZO lengthen the low-field plateau and induce a rounder, less field-dependent high-field region to $J_c(B)$ curve.

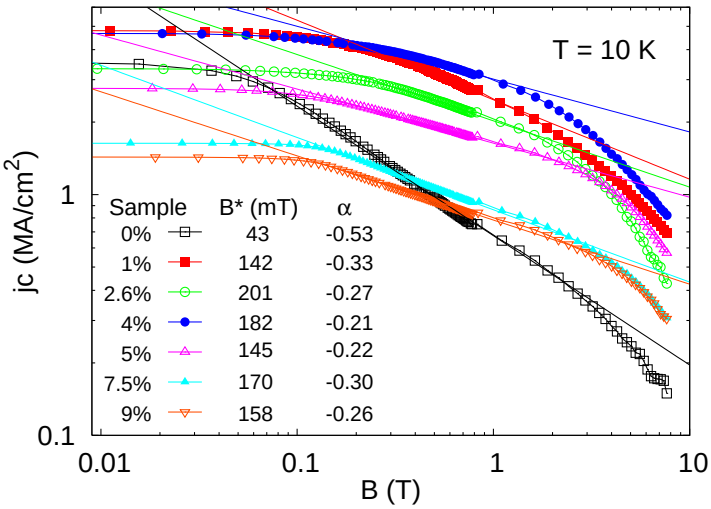

Figure 31. Magnetic field dependence of J_c (labelled as j_c) for BZO+n-films on STO determined from the hysteresis loops at 10 K. The lines are the fits to equation 8. The inset table shows the accommodation field values B^* and the power-law exponents in fits to equation 8.

3.2.4 Accommodation field B^*

The accommodation field, B^* (equation 7), was found to decrease with increasing Pr concentration in all the Pr-doped samples [**P1**]–[**P2**] on STO, MgO and NiW substrates, as presented in figure 32a. For samples on MgO and NiW a clear inverse correlation between the lattice coherence length, r_c, and B^* can be observed. A long r_c corresponds to a better ordering of the lattice and a smaller amount of lattice defects functioning as pinning sites. Therefore, the decrease in B^* with increasing Pr concentration is expected. Also, because GB's act as 2D-APC's, it is qualitatively evident that B^* decreases if J_c^{gb} increases, because in the GB regions SC properties are improved. For samples on buffered NiW, the B^* values are roughly two times higher than in samples on MgO, which can also be seen from the different shapes of the $J_c(B)$ curves in figure 28 between samples on MgO and NiW substrates. The higher B^* values in samples on NiW can be explained by a higher number of lattice defects, e.g. GB's and other pinning sites, than in samples on MgO, as very short r_c's in samples on NiW indicate.

For BCO-doped samples [**P3**] B^* was found to increase, as seen in figure 33a, giving the highest value 218 mT at 10 K with the highest doping level, 10 wt%, which had the

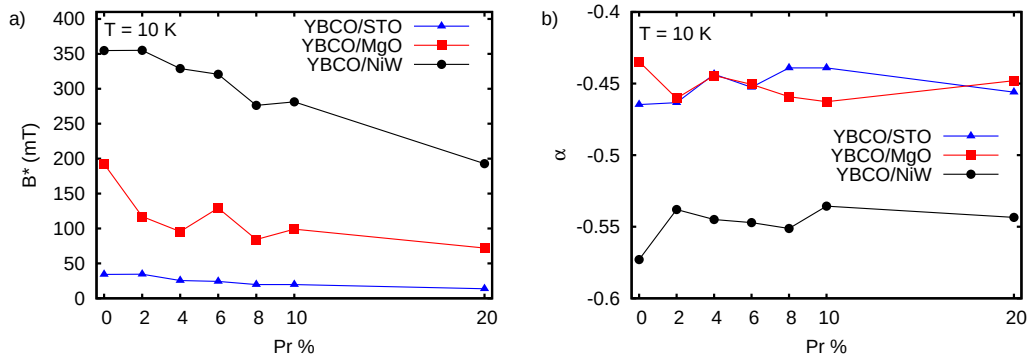

Figure 32. a) Accommodation field B^* and b) power law exponent α at 10 K for all Pr-doped samples on STO, MgO and buffered NiW substrate. a) B^* decreases in all the Pr-doped samples (excluding 2% doped sample on NiW, where the value remains the same), compared with the undoped ones. b) α varies between -0.4 and -0.5 in all the samples on STO and MgO and between -0.5 and -0.6 in samples on NiW without clear correlation to the Pr concentration.

shortest r_c and an inverse correlation was observed between B^* and r_c, as expected. B^* of the undoped sample was the lowest at all the temperatures, whereas 10 wt% doped samples B^* was the highest up to 60 K. Between 70–80 K the highest B^* was observed with the 4 wt% doped sample. This behavior is comparable with BZO-doped samples on STO [**P5**]–[**P6**]. However, whereas the B^* increased systematically in BZO-doped samples, no clear linear dependence between B^* and BCO concentration can be detected. In BZO-doped samples, the highest B^* was measured with the highest dopant concentration (9 wt%), as seen in figure 34, or between 2.6 wt% and 4 wt%, which is close to the magnetically observed n_{opt}, as presented in figure 31.

For BZO+n-YBCO films grown on both STO and NiW, B^* and α values are presented in figure 34. The values of B^* are clearly higher in films deposited on NiW than on STO at BZO concentrations up to 7.5 wt%. Because higher B^* is associated with a higher density of correlated defects [48], we can conclude that in samples on STO there are not very many other defects than BZO and a relatively high B^* already in undoped YBCO on NiW indicates significant amount of structural defects even in the undoped films. This observation goes well with the structural results, and the B^* value is essentially the same as the observed B^* for undoped μ-YBCO on NiW in [**P2**]. This indicates that the distorting effect of NiW substrate overrides the observed excess of

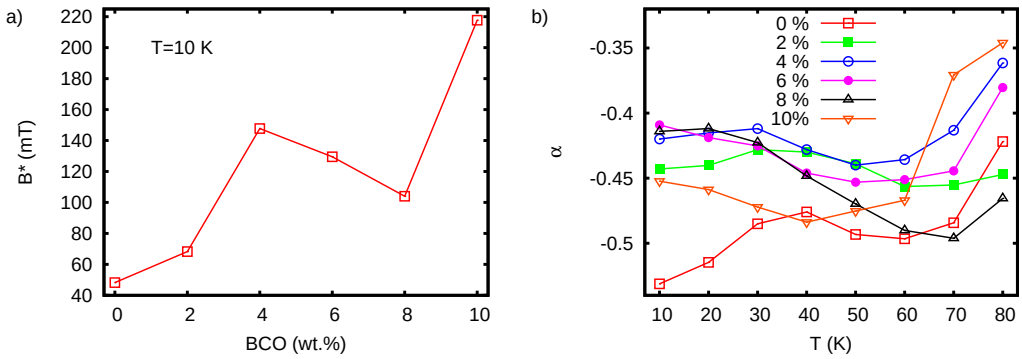

Figure 33. a) Accommodation field B^* at 10 K was found to increase in all the doped samples without clear correlation to BCO content giving its highest value, 218 mT, with the highest doping level 10 wt% BCO at 10 K. b) Power law exponent α in all temperatures for all BCO-doped samples. The difference in α between undoped and doped samples is especially clear at low temperatures, indicating altered pinning dynamics with doped samples.

lattice defects in n-YBCO samples [25]. Also, for BZO-doped films in [**P6**] B^* had a clear inverse correlation with r_c.

B^* decreased in all the Pr-doped samples on all the substrates, whereas in BaMO$_3$-doped (M = Ce, Zr) samples B^* increased in all the doped samples on STO. In Pr-doped samples, this is connected to the increase of J_c^{gb} at low dopant concentrations and decrease in pinning site density as r_c increases. However, in BaMO$_3$-doped samples the increased B^* is due to correlated defects (n+BZO) and overall increase in pinning site density (n+BZO and BCO).

3.2.5 Power law exponent α

In the following, the α values are presented in absolute values.

For Pr-doped samples [**P1**]–[**P2**], the power law exponent α, presented at 10 K in figure 32b, varies between 0.3 and 0.5 and decreases with increasing temperature in all the samples on STO and MgO. The 20% doped sample presents an exception between 60 K and 70 K, where α increases notably. However, this is due to the proximity of the T_c in the 20% sample, which complicates the power law fitting. For Pr-doped samples on NiW, the power law exponent α varies between 0.5 and 0.8 without clear correlation to the Pr concentration. Above 30 K, α is slightly increased in the doped samples, but

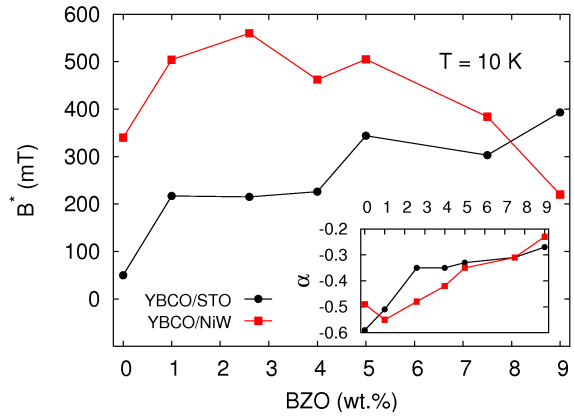

Figure 34. Accommodation field B^* measured at 10 K and the power-law exponent α (inset) for BZO+n-YBCO films grown on both STO and NiW substrates.

all the samples indicate a low density of strong pinning centers.

Determined α-values for BCO-doped samples [**P3**] are presented in figure 33b. The values vary mainly between 0.4 and 0.55 up to 80 K, excluding the 10 wt% doped sample, which is already almost above the irreversibility line at 80 K. The difference between undoped and doped samples is especially clear at low temperatures. The undoped sample is clearly in $\alpha = 0.5$ region up to 70 K, while the 2 wt% - 6 wt% samples are closer to $\alpha = 0.4$, which is in accordance with literature for randomly distributed nanoparticles [27]. All the samples (excluding the 2 wt% BCO-doped) seem to improve their pinning properties above 70K. This increase of α arises from the difficulty in the correct fit of α when the linear part of the log-log $J_c(B)$ is not very prominent. However, compared with BZO the values of α are larger with BCO, which is expected as the relative increase in $J_c(B)$ is smaller with BCO than BZO.

For BZO-doped samples [**P6**], the value of α (inset in figure 34) decreases in samples on STO from 0.6 to around 0.3 for BZO concentration of 2.6 wt% being almost constant above that. Still, in films on NiW, α decreases almost linearly with BZO concentration from about 0.55 at 0 wt% of BZO to around 0.25 at BZO 9 wt%. It is notable, that the films on STO reach a more effective and strong vortex pinning ($\alpha \approx 0.3$) with lower BZO concentrations than in films on NiW. This shows that n_{opt} is higher for BZO-doped YBCO on NiW than on STO. For the BZO-doped samples in [**P5**], presented in figure 31, α is 0.53 for the undoped sample, which is in agreement with theories [49, 64, 65]. For doped samples α varies between 0.21–0.33, which fits with

the structural results where twin boundaries, dislocations and BZO nanorods cause the increase in J_c and the different shape for the $J_c(B)$-curves for BZO-doped samples.

In summary, in the Pr-doped samples where J_c is increased, compared with the undoped sample, no additional strong pinning sites nor a change in the pinning dynamics can be concluded according to B^* and α. However, in BCO- and BZO-doped samples improved pinning properties are observed. For BCO-doped samples the improvement is clear at low temperatures but especially above 30 K the shape of the $J_c(B)$ curve complicates the fitting of equation 8. Nevertheless, in BZO-doped samples the α values indicate strong pinning, which is expected with correlated defects and nanorods that BZO induces into YBCO lattice. Above 5 wt% of BZO α starts to increase [**P5**], indicating a change in the pinning dynamics. This can be explained by single particles forming together with BZO nanorods. Furthermore, it has been reported that the c-axis correlated peak in $J_c(\theta)$ decreases when the amount of BZO exceeds 4 wt% [114], which also indicates a combination of different types of defects responsible for pinning in higher dopant concentrations.

3.2.6 Angular dependence of J_c

The angular dependence of J_c was measured for all the BCO-doped samples in [**P3**], to determine the shape of the $J_c(\theta)$ and to study the effect of BCO to γ_{eff}. As a result, none of the samples presented any c-axis peak in the $J_c(\theta)$ curves. Figure 35 presents the angular dependency of J_c for the 2 wt% BCO-doped sample at 30 K. Only the characteristic concave shape with a peak at $B \parallel ab$ ($\theta = 90^\circ$ and 270°), which is typical for undoped μ-YBCO films [**P4**] [35] can be detected. However, γ_{eff} was found to be 2.2 in BCO-doped samples, which indicates decreased anisotropy compared with the undoped μ-films $\gamma_{\text{eff}} = 5-7$ [35]. This result is in line with literature, where YBCO thin films with BZO nanoparticles have $\gamma_{\text{eff}} = 2.8$ [122]. These results, combined with structural and magnetic data, show that in PLD thin films of YBCO, the BCO-doping causes an isotropic increase in pinning and this is due to randomly distributed BCO-nanoparticles, acting as 3D-APC's.

For the μ-, n- and BZO+n films [**P4**] the $J_c(T, \theta)$ parallel ($\theta = 0^\circ$) and perpendicular ($\theta = 90^\circ$) to the YBCO c-axis were found to be the highest for the BZO+n film in the whole magnetic field range and at all temperatures. Figure 36 presents an example of these values, measured in 4 T. As observed, the μ-film has the lowest values on both directions, excluding 50–80 K where $B \parallel c$ values are similar to n-film. However, the relative differences between B parallel and perpendicular to c-axis are similar between

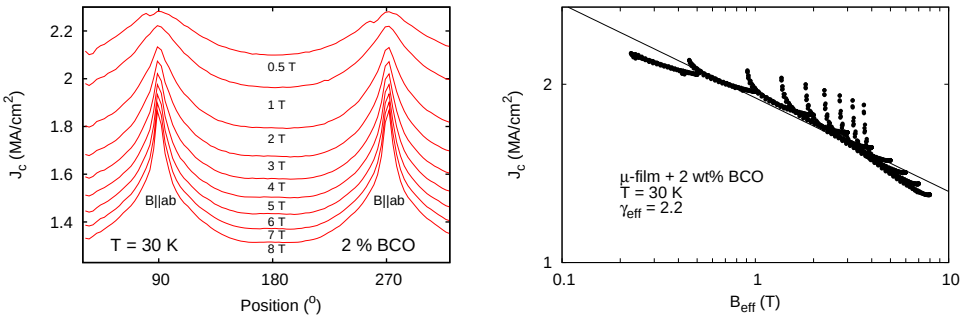

Figure 35. The angular dependence of J_c for 2 wt% BCO-doped sample at 30 K in external magnetic fields between 0.5 T–8 T. As for all the BCO-doped samples, no c-axis peak can be detected. Data falls into a line with $\gamma_{\rm eff} = 2.2$. The line is the J_c dependence with $B_{\rm eff}$ obtained from the collapsed regions.

μ- and n-film and $J_{\rm c}(T, 90°)$ is always higher than the $J_{\rm c}(T, 0°)$, though n-film has higher J_c values in general. In contrast, for the BZO+n film the difference between the $J_{\rm c}(T, 0°)$ and $J_{\rm c}(T, 90°)$ is smallest in the whole temperature and magnetic field range and in 4 T there is a crossover at 50 K, as seen in figure 36. This crossover temperature was found to increase with the increasing magnetic field.

The μ-film has the typical concave shape of $J_{\rm c}(\theta)$ for undoped YBCO film [35], whereas the n-films curve is flatter with a sharp peak at the $B \parallel ab$ ($\theta = 90°$). On the other hand, the BZO-n-film has a very wide peak at $B \parallel c$ at the low-field region, which disappears at high fields and temperatures. This transition to concave shape takes place above B_ϕ where porous vortex solid forms [76] and therefore the c-axis oriented peak disappears. From the Blatter scaling (equation 11) we obtain $\gamma_{\rm eff} = 5$ for the μ-film (see figure 37), which is again in the typical range of $\gamma_{\rm eff}$ =5–7 for undoped YBCO μ-thin film [35]. However, the n-film collapses to a line with $\gamma_{\rm eff} = 1.8$ and BZO+n-film does not collapse to a line at any $\gamma_{\rm eff}$ value at low temperatures, and therefore figure 37 presents BZO+n data at 70 K. Insets in figure 37 present the nonscaling with $\gamma_{\rm eff} = 5$ for these two n-films. Indeed, though n-film is phase pure YBCO, it has notably lower effective J_c anisotropy than the μ-film, which is due to excess amount of correlated pinning sites. For BZO+n-film, the nonscaling is caused by the c-axis correlated BZO rods, observed in most BZO-doped films and also in BZO+n-films [25]. Obviously, these nanorods cause the wide peak at $B \parallel c$ ($\theta = 0°$) in the $J_{\rm c}(\theta)$ curves.

When the collapsed lines in figure 37 are deconvoluted to the $J_{\rm c}(\theta)$ curves, the

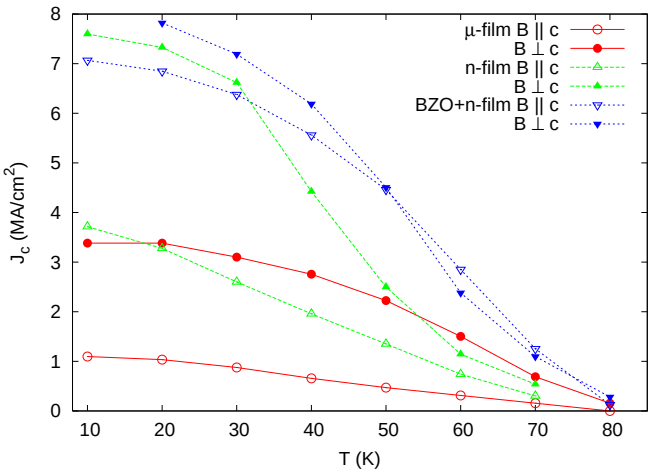

Figure 36. $J_c(T)$ parallel and perpendicular to the c-axis at 4 T for the μ, n, and BZO+n films. The difference between the $J_c(T, 0°)$ and $J_c(T, 90°)$ is smallest for the BZO+n film in the whole temperature range.

μ- and n-film fits follow the measured data nicely, as expected, excluding the $B \parallel ab$ ($\theta = 90°$) peak, which is due to intrinsic pinning and lattice defects in the plane of the film. The BZO+n film curve agrees to the expected shape from the Blatter scaling theory only above 6 T, because the normal concave shape appears only at high fields and temperatures. Results indicate that the n- and the BZO+n-YBCO thin films have a greatly decreased angular anisotropy of J_c. Moreover, as the μ-YBCO thin film follows nicely the random pinning site model and its $\gamma_{\text{eff}} = 5$ is in the normal range, this difference indicates effective pinning sites in both n- and BZO+n-films. The BZO rods are the obvious pinning sites in the BZO+n-films, and the excess number of dislocations in both n-films compared to μ-films [25, 123] lead to more c-axis oriented pinning.

3.2.7 High-field J_c

The resistivity measurements with pulse magnet setup were done for YBCO BZO+n-films on STO. The pinning potential values $U(B, T)$, presented in table 6, were calculated with equation 10 from the temperature dependence measurements of $\rho(B)$. As table 6 indicates, the fitted pinning energy values increase with BZO doping. The $U(B)$ values for the undoped sample at 65 K are in line with earlier results [124, 125], together with doped samples, which are in agreement with earlier study with $BaSnO_3$ and BZO [125]. The field dependences of the J_c of the undoped and BZO-doped YBCO

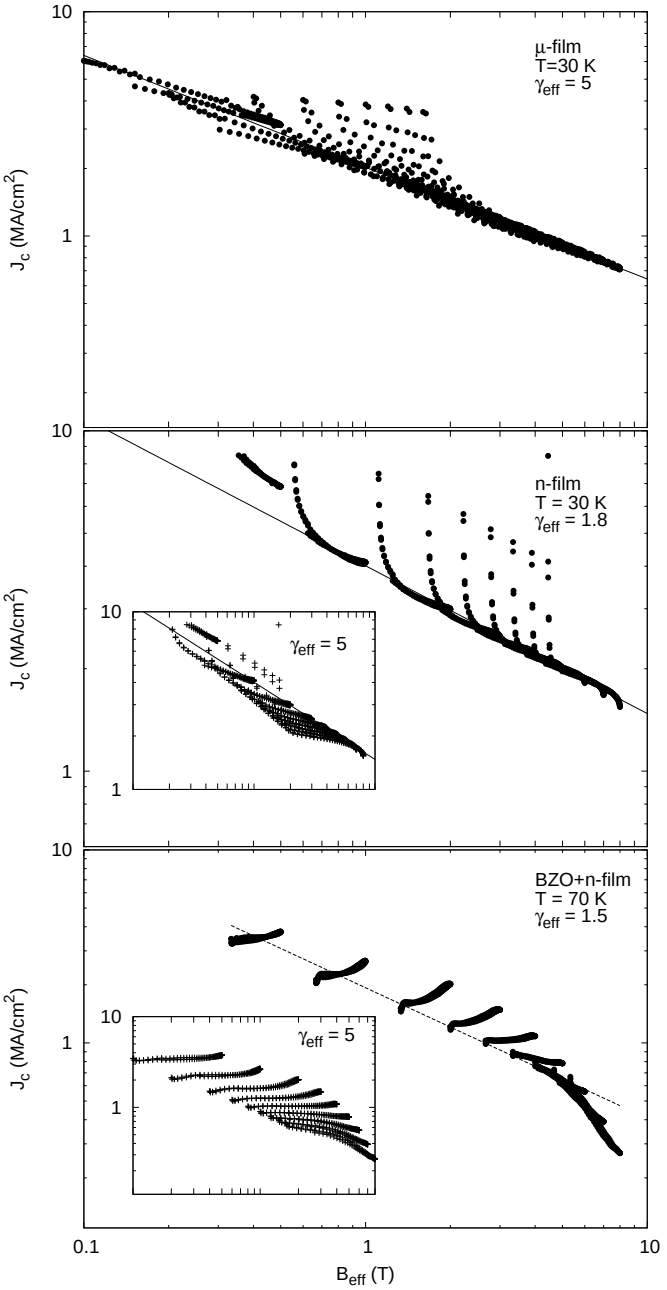

Figure 37. The scaling of the $J_{\rm c}(B,\theta)$ data for the μ-, n-, and BZO+n-films. Note that the BZO+n-film data are taken at 70 K, whereas the others are at 30 K. The insets show scaling with $\gamma_{\rm eff}$ =5 for the n and BZO+n films.

Table 6. Temperature dependence of the pinning potential values $U(B,T)$ calculated from the fitted U_0 and α values at 15 T for the undoped (0 wt%) and BZO-doped (19 wt%) YBCO films.

Sample (%)	U(15 T, 65 K) (K)	U(15 T, 77 K) (K)	U(15 T, 88 K) (K)
0	561	30	1
1	913	73	2
2.6	1104	73	3
4	756	48	3
5	913	73	7
7.5	938	73	7
9	1532	126	-

films at 65 K are presented in figure 38a. All the BZO-doped YBCO films have higher J_c's than the undoped sample in this high magnetic field range. However, there is no clear correlation between BZO content and J_c, but it is notable that higher BZO contents are more effective when compared with the J_c's obtained from magnetic measurements, e.g. 9 wt% BZO-doped sample has the highest J_c above 23 T (figure 38a), while the same sample had the smallest magnetically measured J_c below 0.6 T (figure 30). Moreover, the B_{irr}'s, presented in figure 38b, determined from the $\rho(B)$ curves point where ρ exceeds the noise level $3 \cdot 10^{-7}$ Ωm, show that the solid-liquid transition of the vortex matter occurs 5 T higher for the 9 wt% BZO-doped sample than in the undoped sample at $T/T_c < 0.9$. In all the other samples irreversibility lines are located in between the 0 and 9 wt% doped samples. This notable difference in n_{opt} between low-field and high-field region is due to the field dependence of the n_{opt}. This dependence is presented in figure 39. As observed, the n_{opt} is almost constant between 1–20 T, but above this range the maximum position of $J_c(n)$ (inset in figure 39) changes. Because the density of the columnar defects does not increase linearly with dopant concentration, it is understandable that a higher n_{opt} is needed in the high magnetic field region. This increase can be qualitatively explained with a model where isotropic pinning sites are formed in addition to nanorods.

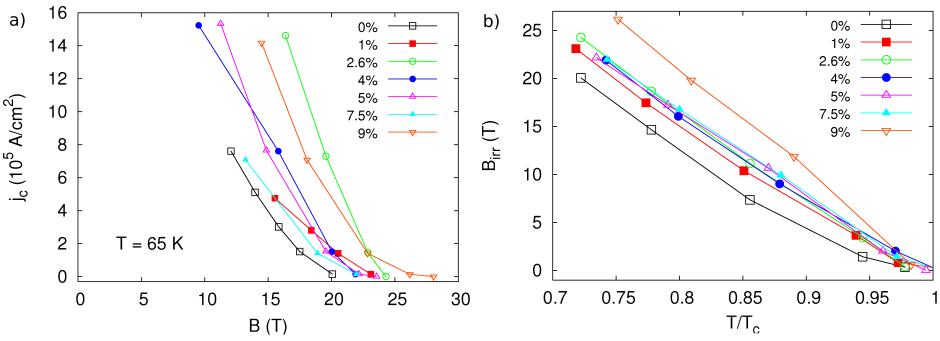

Figure 38. a) The field dependences of the J_c's at 65 K and b) the temperature dependence of B_{irr} for BZO-doped YBCO thin films determined from the pulsed magnetic field data [**P5**].

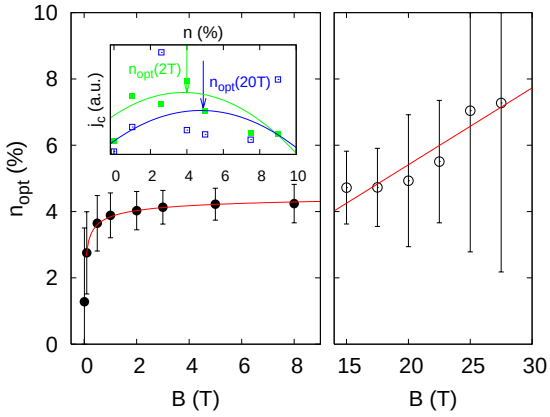

Figure 39. Magnetic field dependence of optimal BZO concentration n_{opt} measured in two different field ranges. The error bars are calculated from the parabolic fits to the experimental BZO concentration dependent J_c data, measured at different magnetic fields. The lines in the main panels are fits to the exponential increase in low fields on the left and to the linear behavior on the right.

4 Conclusions

"Shall I refuse my dinner because I do not fully understand the process of digestion?"
–Oliver Heaviside

In this work, three different doping methods of YBCO thin films have been studied, leading to three different mechanisms to increase the critical current density, J_c, in pulsed laser deposited YBCO thin films.

For cationic inclusion, Pr^{3+} (Pr) at the Y^{3+} site, the effect of increasing J_c is connected to an increase in the grain boundary critical current density J_c^{gb}. This is evidenced by the fact that in the absence of GB's (samples on STO), J_c does not increase with Pr, whereas in Pr-doped samples on MgO and buffered NiW, both T_c and J_c increased in low dopant levels. The highest J_c's were achieved in 2% Pr-doped samples at all temperatures and fields in samples on buffered NiW, and in the self-field (0 T) at all temperatures, and in all fields above 60 K in samples on MgO. The dependence of T_c on Pr concentration indicates that the intra-grain inhomogeneity does not increase until 10% of Pr. This can be explained by Pr segregating into the grain boundary regions, increasing J_c^{gb} by increasing the O vacancy formation energies, reducing hole depletion and increasing carrier density, accordingly, inducing the same mechanism as Ca^{2+} has been shown to induce [98, 101]. Excess O vacancies in grain boundaries and their corollary effects are the primary reason for the reduction in J_c in poly-crystalline YBCO. Pr doping decreases the intrinsic excess of O vacancies of YBCO grain boundaries. Thus, high critical currents are restored through a cooperative doping mechanism. Furthermore, the results indicate that in the grain boundary regions under compression and tension, Pr also replaces Ba, which relieves strain and again suppresses O vacancies. Moreover, in the presence of GB's, the lattice coherence length increased in doped samples among with the structural quality in the c-axis direction. According to the results from B^* and α the pinning dynamics did not change substantially in samples on any substrate. These results are in line with literature, where Pr inclusion has been found to increase J_c e.g. in bulk [15, 93, 126] and melt-textured samples [127], where in all cases GB's are present.

The effect of doping with the non-superconducting perovskites $BaCeO_3$ (BCO) and $BaZrO_3$ (BZO) was found to be different. According to the structural measurements, the BCO is distributed into the lattice as very small particles, with an estimated size of 2 nm. The surface microstructure of the films changed with increasing BCO content,

from a regular grain size and distribution to an irregular one, already visible at 4 wt% of BCO, which is in line with observations on melt-textured and bulk samples [19, 20]. However, the twin structure can be clearly seen in XRD even in the 10 wt% BCO-doped sample indicating less lattice distortion compared with the BZO dopant.

J_c was found to increase and, depending on the external field and temperature, the highest J_c's were obtained with 2 wt% or 4 wt% BCO-doped samples. The $J_c(B)$ curve sits between the undoped and optimally BZO-doped sample below 80 K. Only at 80 K the 2 wt% BCO-doped sample gave higher J_c values in the whole field region than the optimally doped (4 wt%) BZO sample. BCO doping was found to decrease the $J_c(\theta)$ anisotropy notably to $\gamma_{\text{eff}} = 2.2$. The determined B^* and α, together with the structural and angular dependency measurements of J_c indicate a different type of pinning dynamics compared with BZO. We propose that this is due to the roundish, randomly distributed small BCO particles (3D-APC's), not columnar defects, in the YBCO lattice.

In contrast, in the BZO-doped samples, BZO grows cube-on-cube with YBCO, forming a correlated network of film penetrating nanorods (1D-APC's). Also, the thin films ablated from a n-grained and a BZO-doped n-grained YBCO target have a greatly decreased angular anisotropy of J_c. Because the thin film ablated from μ-grained YBCO follows nicely the random pinning site model and its $\gamma_{\text{eff}} = 5$ is in the normal range, this difference indicates effective pinning sites in both n- and BZO+n-films. The BZO rods are the obvious pinning sites in the BZO+n films and more dislocations in both n-films than in μ-film [25, 123] lead to more c-axis oriented pinning. However, as we observe in [**P5**] α increases above 5 wt% of BZO, which complicates the pinning system. This can be explained by a combination of c-axis oriented pinning and single particles forming together in the lattice above 5 wt% of BZO. The optimal BZO concentration increases above 20 T from 4 wt% almost up to 8 wt%. This increase can be explained with a model where isotropic pinning sites are formed in addition to nanorods.

When we compare the results from thin films deposited on single crystal STO and buffered NiW, we can conclude that while the optimal BZO concentration depends on temperature and field, n_{opt} is a few wt% higher in films on NiW than in films on STO. This is in agreement with earlier results [25], where differences in defect densities between the undoped n- and μ-films have been observed to be important when the BZO dopants are distributed into the YBCO lattice.

In conclusion, all the studied dopants did increase J_c, but the substrate, the temperature and the magnetic field range determine the optimal dopant concentration.

References

[1] H. Onnes, Leiden Comm. **120b, 122b, 124c**, (1911).

[2] W. Meissner and R. Ochsenfeld, Naturwissenschaft **21**, 787 (1933).

[3] F. London and H. London, Physica **2**, 341 (1935).

[4] V. L. Ginzburg and L. D. Landau, Zh. Eksp. Teor. Fiz. **20**, 1064 (1950).

[5] J. Bardeen, L. N. Cooper and J. R. Schrieffer, Physical Review **108**, 1175 (1957).

[6] J. G. Bednorz and K. A. Müller, Z. Phys. B **64**, 189 (1986).

[7] M. K. Wu *et al.*, Phys. Rev. Lett. **58**, 908 (1987).

[8] J. Nagamatsu *et al.*, Nature **410**, 63 (2001).

[9] Y. Kamihara *et al.*, J. Am. Chem. Soc. **128**, 10012 (2006).

[10] R. Wesche, *Springer Handbook of Electronic and Photonic Materials* (Springer, 2006).

[11] N. Klein *et al.*, J. Appl. Phys. **67**, 6940 (1990).

[12] W. V. Hasselzahl *et al.*, Proceedings of the IEEE **92**, 1655 (2004).

[13] P. Lahl and R. Wördenweber, J. Appl. Phys. **97**, 113911 (2005).

[14] C. P. Poole, H. Farach, R. Creswick and R. Prozorov, *Superconductivity, Second Edition* (Academic Press, 2007).

[15] H. Huhtinen *et al.*, Supercond. Sci. Technol. **20**, S159 (2007).

[16] G. Hammerl *et al.*, Nature **407**, 162 (2000).

[17] A. Schmehl *et al.*, Europhysics Letters **47**, 110 (1999).

[18] K. Guth, H. U. Krebs, H. C. Freyhardt and C. Jooss, Phys. Rev. B **64**, 140508 (2001).

[19] A. Mahmood *et al.*, Physica C **468**, 1355 (2008).

[20] A. Mahmood *et al.*, Physica C **469**, 1165 (2009).

[21] S. Nariki, N. Sakai, M. Murakami and I. Hirabayashi, Physica C **426-431**, 602 (2005).

[22] Y. Kim *et al.*, Supercond. Sci. Technol. **22**, 065010 (2009).

[23] Y. H. Kim *et al.*, Physica C **469**, 1410 (2009).

[24] O. V. Boytsova, A. R. Kaul, S. V. Samoilenkov and I. E. Voloshin, Journal of Physics: Conference series **234**, 012008 (2010).

[25] M. Peurla *et al.*, IEEE T. Appl. Supercond. **17**, 3608 (2007).

[26] J. L. MacManus-Driscoll *et al.*, Nat. Mater. **3**, 439 (2004).

[27] B. Maiorov *et al.*, Nat. Mater. **8**, 398 (2009).

[28] M. Peurla *et al.*, Phys. Rev. B **75**, 184524 (2007).

[29] K. Matsumoto and P. Mele, Supercond. Sci. Technol. **23**, 014001 (2010).

[30] U. Welp *et al.*, Phys. Rev. Lett. **62**, 1908 (1989).

[31] H. Casalta *et al.*, Physica C **258**, 321 (1996).

[32] L. Krusin-Elbaum *et al.*, Phys. Rev. B **39**, 2936 (1989).

[33] A. Mourachkine, *High-temperature superconductivity in cuprates* (Kluwer Academic Publishers, 2002).

[34] I. E. Trofimov *et al.*, Journal of Superconductivity **7**, 209 (1994).

[35] J. Gutiérrez, T. Puig and X. Obradors, Appl. Phys. Lett. **90**, 162514 (2007).

[36] L. Civale *et al.*, IEEE T. Appl. Supercond. **15**, 2808 (2005).

[37] G. Blatter *et al.*, Rev. Mod. Phys. **66**, 1125 (1994).

[38] J. Sarrao and W.-K. Kwok,
Basic Research Needs for Superconductivity (U.S. Department of Energy, 2006),
`www.er.doe.gov/bes/reports/files/sc_rpt.pdf`.

[39] S. R. Foltyn *et al.*, Nat. Mater. **6**, 631 (2007).

[40] T. Haugan *et al.*, Nature **430**, 867 (2004).

[41] Y. Yamada *et al.*, Appl. Phys. Lett. **87**, 132502 (2005).

[42] A. Crisan *et al.*, Appl. Phys. Lett. **79**, 4547 (2001).

[43] T. Aytug *et al.*, J. Appl. Phys. **98**, 114309 (2005).

[44] K. Matsumoto *et al.*, Physica C **412-414**, 1267 (2004).

[45] J. C. Nie *et al.*, Supercond. Sci. Technol. **17**, 845 (2004).

[46] T. Schuster *et al.*, Phys. Rev. B **47**, 373 (1993).

[47] L. Civale *et al.*, Phys. Rev. Lett. **67**, 648 (1991).

[48] B. Dam *et al.*, Nature **399**, 439 (1999).

[49] F. C. Klaassen *et al.*, Phys. Rev. B **64**, 184523 (2001).

[50] V. M. Pan, A. L. Kasatkin, V. L. Svetchnikov and H. W. Zandbergen, Cryogenics **33**, 21 (1993).

[51] C. Jooss, R. Warthmann and H. Kronmuller, Phys. Rev. B **61**, 12433 (2000).

[52] M. Daeumling, J. M. Seuntjens and D. C. Larbalestier, Nature (London) **346**, 332 (1990).

[53] V. A. Maroni, Y. Li, D. M. Feidmann and Q. X. Jia, J. Appl. Phys. **102**, 113909 (2007).

[54] L. Civale, Supercond. Sci. Technol. **10**, A11 (1997).

[55] S. R. Foltyn *et al.*, Appl. Phys. Lett. **87**, 162505 (2005).

[56] C. P. Bean, Phys. Rev. Lett. **8**, 250 (1962).

[57] C. P. Bean, Reviews of Modern Physics **36**, 31 (1964).

[58] H. P. Wiesinger, F. M. Sauerzopf and H. W. Weber, Physica C **203**, 121 (1992).

[59] A. Sanchez and C. Navau, Supercond. Sci. Technol. **14**, 444 (2001).

[60] J. Hudner *et al.*, Supercond. Sci. Technol. **7**, 195 (1994).

[61] D. R. Nelson and V. M. Vinokur, Phys. Rev. B **48**, 13060 (1993).

[62] E. Mezzetti *et al.*, Phys. Rev. B **60**, 7623 (1999).

[63] C. Cai *et al.*, Phys. Rev. B **69**, 104531 (2004).

[64] C. J. van der Beek *et al.*, Phys. Rev. B **66**, 24523 (2002).

[65] G. Blatter, V. B. Geshkenbein and J. A. G. Koopmann, Phys. Rev. Lett. **92**, 067009 (2004).

[66] P. Paturi, M. Irjala, A. B. Abrahamsen and H. Huhtinen, IEEE T. Appl. Supercond. **19**, 3431 (2009).

[67] Y. Z. Zhang *et al.*, Phys. Rev. B **71**, 052502 (2005).

[68] G. Blatter, V. B. Geshkenbein and A. I. Larkin, Phys. Rev. Lett. **68**, 875 (1992).

[69] N. J. Long, N. M. Strickland and E. F. Talantsev, IEEE T. Appl. Supercond. **17**, 3684 (2007).

[70] N. J. Long, Supercond. Sci. Technol. **21**, 025007 (2008).

[71] P. Paturi, Supercond. Sci. Technol. **23**, 025030 (2010).

[72] A. Diaz, L. Mechin, P. Berghuis and J. E. Evetts, Phys. Rev. Lett. **80**, 3855 (1998).

[73] L. Civale *et al.*, Appl. Phys. Lett. **84**, 2121 (2004).

[74] A. Palau *et al.*, Phys. Rev. Lett. **97**, 257002 (2006).

[75] M. Peurla *et al.*, Supercond. Sci. Technol. **19**, 767 (2006).

[76] S. S. Banerjee *et al.*, Phys. Rev. Lett. **90**, 87004 (2003).

[77] J. Gutiérrez *et al.*, Nature materials **6**, 367 (2007).

[78] A. V. Narlikar, C. V. N. Rao and S. K. Agarwal, *Studies of High Temperature Superconductors vol 1, ed A Narlikar* (New York: Nova Science, 1989).

[79] A. V. Narlikar *et al.*, Phil. Mag. Part B **79**, 717 (1999).

[80] V. P. S. Awana and A. V. Narlikar, Phys. Rev. B **49**, 6353 (1994).

[81] V. P. S. Awana, A. Tulapurkar, S. K. Malik and A. V. Narlikar, Phys. Rev. B **50**, 594 (1994).

[82] A. Sedky, A. Gupta, V. P. S. Awana and A. V. Narlikar, Phys. Rev. B **58**, 12495 (1998).

[83] E. Blinov *et al.*, Supercond. Sci. Technol. **10**, 818 (1997).

[84] J. Raittila, H. Huhtinen, P. Paturi and Y. P. Stepanov, Physica C **371**, 90 (2002).

[85] F. C. Wellstood, J. J. Kingston and J. Clarke, J. Appl. Phys. **75**, 683 (1994).

[86] P. Paturi, M. Irjala, H. Huhtinen and A. B. Abrahamsen, J. Appl. Phys. **105**, 023904 (2009).

[87] J. Ye and K. Nakamura, Phys. Rev. B **48**, 7554 (1993).

[88] P. Scherrer, Nachrichten von der Gesellschaft der Wissenschaften zu Gttingen **98**, 394 (1918).

[89] A. Gauzzi and D. Pavuna, Appl. Phys. Lett. **66**, 1836 (1995).

[90] H. Huhtinen, K. Schlesier and P. Paturi, Supercond. Sci. Technol. **22**, 075019 (2009).

[91] F. Fabbri *et al.*, Supercond. Sci. Technol. **13**, 1492 (2000).

[92] B. Dam, J. H. Rector, J. M. Huijbregtse and R. Griessen, Physica C **296**, 179 (1998).

[93] T. Harada and K. Yoshida, Physica C **383**, 48 (2002).

[94] K. Kinoshita *et al.*, Jpn. J. Appl. Phys. **27**, L1642 (1988).

[95] A. Goyal *et al.*, Supercond. Sci. Technol. **18**, 1533 (2005).

[96] R. Kromann *et al.*, J. Appl. Phys. **71**, 3419 (1992).

[97] V. Svetchnikov, V. Pan, C. Træholt and H. Zandbergen, IEEE T. Appl. Supercond. **7**, 1396 (1997).

[98] X. Song *et al.*, Nature Mat. **4**, 470 (2005).

[99] D. M. Feldmann *et al.*, J. Mater. Res. **20**, 2012 (2005).

[100] R. K. Singhal, Mater. Lett. **65**, 825 (2011).

[101] R. F. Klie *et al.*, Nature **435**, 475 (2005).

[102] J. Nam *et al.*, J. Appl. Phys. **97**, 123906 (2005).

[103] A. P. Goncalves *et al.*, Phys. Rev. B **37**, 7476 (1988).

[104] J. Fink, N. Nücker, H. Romberg and M. Alexander, Phys. Rev. B **42**, 4832 (1990).

[105] K. Schlesier, *Superconducting properties and their enhancement in* $REBa_2Cu_3O_{7-\delta}$ *(*RE *= Y and Gd) films prepared by pulsed laser ablation* (University of Turku, 2010).

[106] X. L. Li, J. Gao, H. Y. Wong and Z. H. Mai, Thin Solid Films **489**, 200 (2005).

[107] H. Huhtinen, M. Irjala, P. Paturi and M. Falter, IEEE T. Appl. Supercond. (2010).

[108] C. Cai, B. Holzapfel, J. Hänisch and L. Schultz, Phys. Rev. B **70**, 064504 (2004).

[109] Z. F. Ren, J. H. Wang, D. J. Miller and K. C. Goretta, Physica C **229**, 137 (1994).

[110] Z. G. Ivanov *et al.*, Appl. Phys. Lett. **59**, 3030 (1991).

[111] N. F. Heinig, R. D. Redwing, J. E. Nordman and D. C. Larbalestier, Phys. Rev. B **60**, 1409 (1999).

[112] D. Dimos, P. Chaudhari, J. Mannhart and F. K. LeGoues, Phys. Rev. Lett. **61**, 219 (1988).

[113] A. Goyal *et al.*, Supercond. Sci. Technol. **18**, 1533 (2005).

[114] S. Kang *et al.*, Physica C **457**, 41 (2007).

[115] Y. Yeshurun, A. P. Malozemoff and A. Shaulov, Rev. Mod. Phys. **68**, 911 (1996).

[116] R. Goswami *et al.*, Physica C **470**, 318 (2010).

[117] H. Huhtinen *et al.*, Physica C **470**, S1013 (2010).

[118] A. Kiessling *et al.*, Supercond. Sci. Technol. **24**, 055018 (2011).

[119] K. Traito *et al.*, Phys. Rev. B **73**, 224522 (2006).

[120] H. Huhtinen *et al.*, IEEE T. Appl. Supercond. **17**, 3620 (2007).

[121] Y. V. Fedotov *et al.*, Physica C **372-376**, 1091 (2002).

[122] A. Palau *et al.*, IEEE T. Appl. Supercond. **21**, 3243 (2011).

[123] P. Paturi, M. Peurla, K. Nilsson and J. Raittila, Supercond. Sci. Technol. **17**, 564 (2004).

[124] T. L. Hylton and M. R. Beasley, Phys. Rev. B **41**, 11669 (1990).

[125] P. Mele *et al.*, Supercond. Sci. Technol. **21**, 032002 (2008).

[126] L. M. Paulius, C. C. Almasan and M. B. Maple, Phys. Rev. B **47**, 11627 (1993).

[127] H. T. Ren *et al.*, Physica C **216**, 447 (1993).